CHEMISTRY OF MATERIALS
Cite This: Chem. Mater. 2020, 32, 805−820
Article
pubs.acs.org/cm

Structure−Charge Transport Relationships in Fluoride-Doped Amorphous Semiconducting Indium Oxide: Combined Experimental and Theoretical Analysis

Aritra Sil,[†] Laleh Avazpour,[#,§] Elise A. Goldfine,[‡] Qing Ma,[∥] Wei Huang,[†] Binghao Wang,[†] Michael J. Bedzyk,[*,‡] Julia E. Medvedeva,[*,§] Antonio Facchetti,[*,†,⊥] and Tobin J. Marks[*,†]

[†]Department of Chemistry and [‡]Department of Materials Science and Engineering, Northwestern University, 2145 Sheridan Road, Evanston, Illinois 60208, United States

[§]Department of Physics, Missouri University of Science and Technology, Rolla, Missouri 65409, United States

[∥]DND-CAT, Northwestern Synchrotron Research Center at the Advanced Photon Source, Argonne, Illinois 60439, United States

[⊥]Flexterra Inc., 8025 Lamon Avenue, Skokie, Illinois 60077, United States

Supporting Information

ABSTRACT: Anion doping of transparent amorphous metal oxide (a-MO) semiconductors is virtually unexplored but offers the possibility of creating unique optoelectronic materials owing to the chemical tuning, modified crystal structures, and unusual charge-transport properties that added anions may impart. We report here the effects of fluoride (F^-) doping by combustion synthesis, in an archetypical metal oxide semiconductor, indium oxide (In−O). Optimized fluoride-doped In−O (F:In−O) thin films are characterized in depth by grazing incidence X-ray diffraction, X-ray reflectivity, atomic force microscopy, X-ray photoelectron spectroscopy, and extended X-ray absorption fine structure (EXAFS). Charge-transport properties are investigated in thin-film transistors (TFTs), revealing that increasing fluoride content (0.0 → 1.57 atom %) slightly lowers the on-current (I_{on}) and electron mobility due to scattering from loosely bound F^- centers but enhances important TFT performance parameters such as the I_{on}/I_{off} ratio, subthreshold swing, and bias stress stability, yielding superior TFT switching versus undoped In−O. These results are convincingly explained by ab initio molecular dynamics simulations and density functional theory electronic structure calculations. Combined with the EXAFS data, the experimental and theoretical results show that F^- hinders crystallization by enhancing the local and medium-range disorder, promotes a uniform film morphology, and favors the formation of deeper, more localized trap states as compared to F^--free In−O. These data also show that the local organization and electronic structure of amorphous F^--doped oxide semiconductors are significantly different from those of F^--doped crystalline oxide semiconductors and suggest new avenues to further modify a-MOs for enhanced optoelectronic properties.

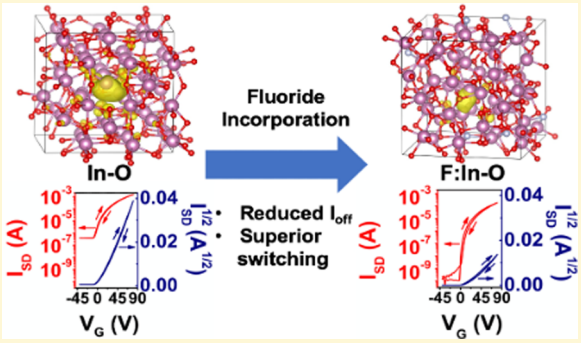

INTRODUCTION

Amorphous metal oxide (a-MO) semiconductors are a unique charge-carrying materials family for flexible, transparent thin-film transistors (TFTs) owing to their high carrier mobility ($\mu \approx 1-100$ cm^2 V^{-1} s^{-1}) in the amorphous state, high optical transparency in the visible region (>85%), great mechanical flexibility, and excellent environmental stability.[1−9] These materials can overcome some of the greatest limitations of conventional semiconductors such as poor morphological and charge-transport uniformity over large areas and the high deposition costs of low-temperature polycrystalline silicon,[10,11] as well as the low carrier mobility ($\mu \approx 0.5-1.0$ cm^2 V^{-1} s^{-1}) and poor optical transparency of amorphous silicon.[12−16] Furthermore, a-MO-based semiconductors offer superior carrier mobility, optical transparency, and robustness versus other unconventional semiconductors such as organic materials.[17−19]

a-MO semiconductors also offer broad tunability with respect to optoelectronic and charge-transport properties, which make them attractive for TFT applications. Currently, much of the tunability has been achieved by doping cations of different chemical properties such as "oxygen-getters" (e.g., Ga^{3+}, Sc^{3+}, Y^{3+}),[1,20−23] late-transition metals (e.g., Zn^{2+}),[24] and s-/p-block elements (e.g., Li^{1+}, Al^{3+}, Sn^{4+})[25−28] in an indium oxide (In−O) matrix. The resulting cation-doped ternary In−X−O (e.g., In−Zn−O, Zn−Sn−O, etc.) and quaternary In−

Received: October 17, 2019
Revised: December 20, 2019
Published: December 20, 2019

DOI: 10.1021/acs.chemmater.9b04257
Chem. Mater. 2020, 32, 805−820

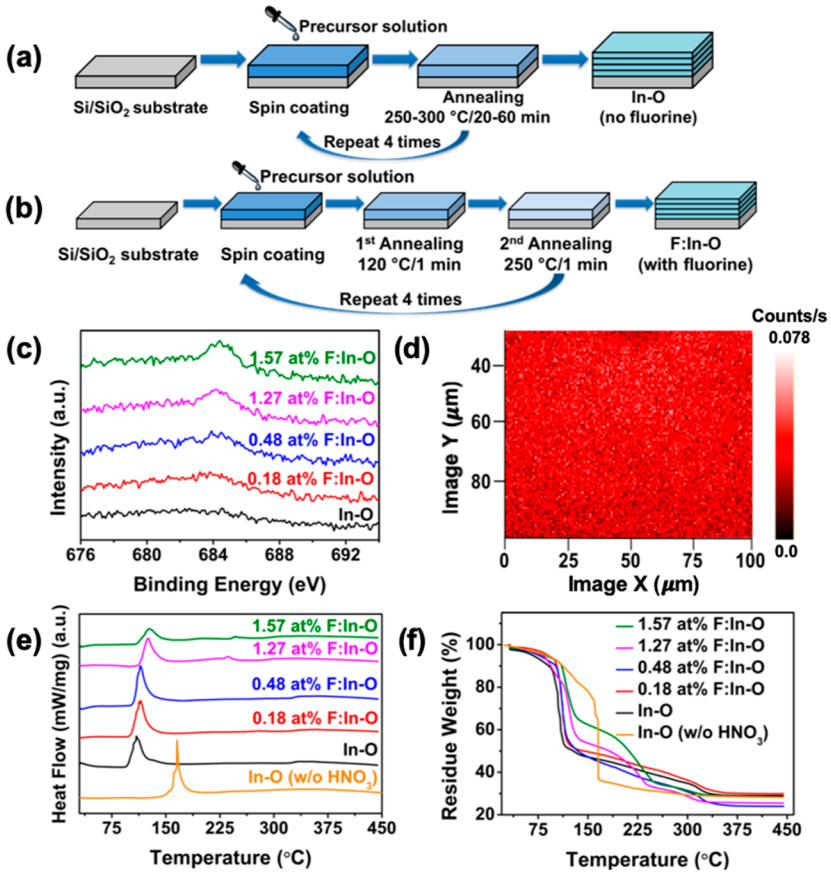

Figure 1. (a) Conventional one-step annealing process for combustion synthesis. (b) Two-step fast annealing process for combustion synthesis. (c) F1s XPS spectra of indicated *x* atom % F:In−O thin films. (d) F1s XPS imaging of 1.27 atom % F:In−O thin film ($R_q \approx 0.158$ nm). (e) DSC analysis, and (f) TGA analysis of vacuum-dried precursor solutions of indicated *x* atom % F:In−O thin films.

X−Y−O (e.g., In−Zn−Ga−O, Zn−In−Sn−O, etc.) materials offer control of film crystallinity,[1,8,13,29−37] electronic localization, carrier mobility, optical band gap, and work function.[20,38,39] Alternatively, insulating polymers can be used to tune the crystallinity, carrier concentration, and work function of In−O as well as other metal oxides (MOs), affording enhanced TFT performance.[40−42]

Another approach to modify MO optoelectronic properties and charge transport is to utilize anions to dope the primary MO matrix via defect and electronic structure variations.[43−45] Moving from nitride to oxide to fluoride increases the metal−anion bond ionic character, widening both the band gap and valence band.[43−45] Among the group 15, 16, and 17 elements, fluoride (F^-) is a promising candidate for anion doping in MOs, since its ionic radius is close to that of oxygen (F^{-1}: 1.285 Å, O^{2-}: 1.35 Å).[46] Note that the field-effect mobility (μ) of indium−gallium−zinc oxide (IGZO) TFTs grown by physical vapor deposition (PVD) (e.g., sputtering, pulsed-laser deposition) is increased by 30−40% on F^- doping.[47−51] In addition, F^- doping enhances the performance of PVD-grown ZnO TFTs and can passivate vacancy defects in Ge-based metal−oxide−semiconductor field-effect transistor (MOSFETs) as well.[52,53] However, PVD techniques are capital-intensive, require vacuum, and provide only line-of-site deposition.[19] Furthermore, F_2 or the other fluoride precursors are toxic, corrosive, and/or contaminate PVD chambers. In contrast, F^--doped ZnO (F:ZnO), F^--doped zinc−tin oxide (F:ZTO), and F^--doped indium−zinc oxide (F:IZO) films are readily grown by sol−gel techniques.[54−56]

Although F^- doping increases TFT mobility, μ = 0.40 $cm^2\ V^{-1}\ s^{-1}$ in F^--doped ZnO (F:ZnO) versus μ = 0.21 $cm^2\ V^{-1}\ s^{-1}$ in undoped ZnO, and increases bias stress stability, the process requires a 250−350 °C annealing for more than 1 h.[54−56] Note that many of these reports[47−51,53−56] are limited in diffraction structural data, accurate F^- quantification, morphology information, and theoretical understanding. Thus, not only is there a need to develop solution (soln)-based, low-temperature growth processes to F^--dope a-MO films but, also, to understand fundamentally the consequences and mechanism of the F^- doping.

This Laboratory recently reported a solution-based, low-temperature, plastic substrate compatible growth technique for MO semiconductor and dielectric films for TFTs—combustion synthesis.[16] Here a fuel and an oxidizer are added to the metal precursor solution. Upon film deposition and thermal annealing, a strong exothermic reaction provides the energy for metal−oxygen−metal (M-O-M) lattice formation and densification. This self-generated heat eliminates the need for high external annealing temperatures, thus enabling TFT fabrication with high carrier mobilities at lower temperatures (250−300 °C) than sol−gel based methods (>400 °C).[2,16,20,57−66] An intriguing question here is whether this methodology is compatible with F^- doping, whether sufficient quantities of the anion can be incorporated into the a-MO structure, and the nature of the resulting film morphological and electronic properties. Fundamentally, we wish to elucidate the effects of F^- on optoelectronic properties, defect structures, and charge transport in *amorphous* indium oxide (In−O) films. Note that

DOI: 10.1021/acs.chemmater.9b04257
Chem. Mater. 2020, 32, 805−820

amorphicity in semiconductors is a desirable property for TFT applications because of the mechanical flexibility and charge transport uniformity it imparts.[19]

In this contribution, we report on the effects of F^- doping in combustion synthesized semiconducting a-MO film matrices, specifically In−O. Growth conditions are optimized to yield fluoride-doped In−O (F:In−O) thin films with F^- incorporation from 0.0 to 1.57 atom %. Grazing incidence X-ray diffraction (GIXRD) and atomic-force microscopy (AFM) probe F:In−O thin-film crystallinity and surface morphology, respectively. X-ray reflectivity (XRR) reveals the thickness, average electron density, and electron density profiles of these films. Charge-transport measurements in thin-film transistors (TFTs) show that, in contrast to previous reports,[47−51,53−56] F^- doping reduces carrier mobility. However, the F:In−O TFTs have lower off-currents, higher I_{on}/I_{off} ratios (10^5), lower subthreshold swing metrics, greater bias stress stability, and thus superior TFT switching properties versus undoped In−O. Ab initio molecular dynamics (MD) simulations and density functional theory (DFT) calculations reveal that F^- doping inhibits crystallization by enhancing the local and medium-range disorders, further confirmed by extended X-ray absorption fine structure (EXAFS) data. The computation further reveals that F^- reduces the electron mobility due to greater carrier scattering and favors the formation of deep localized trap states, thus suppressing I_{off} and increasing optical transparency versus undoped a-In−O. Thus, this work provides a holistic picture of how F^- influences local structure, electronic trap states, and charge-transport properties in amorphous semiconducting MOs and how it differs from the corresponding crystalline matrices.

RESULTS AND DISCUSSION

Combustion Synthesis of Fluoride-Doped Indium Oxide Thin Films. To investigate the feasibility of F^- doping in MOs by thin-film processing via combustion synthesis, several chemical fluoride precursors and fabrication conditions for film deposition were first screened. In−O was chosen as a model system for F^- doping, since it is a simple binary oxide widely used for TFT fabrication.[9,16,67−71] Indium nitrate ($In(NO_3)_3$) was chosen as the metal source and oxidizer, while acetylacetone (AcAcH) is the standard fuel.[2,16,20,57−66] After several trials (Table S1), NH_4F was chosen as the fluoride source, since it is inexpensive and widely used for F^- doping in transparent conducting oxides (e.g., F^--doped tin oxide) by sol−gel processes.[72−78] A small amount of concentrated (conc) HNO_3 (0.35% (v/v)) is added to the combustion precursor solution before film deposition to prevent the formation of insoluble nanoparticles (Figure S1). In preliminary experiments using NH_4F-containing combustion formulations, it was found that annealing the F^--containing thin-film precursors at high annealing temperatures for extended times typical of MO combustion synthesis (250−300 °C for 20−60 min, Figure 1a)[2,16,20,57,59,61−66] does not facilitate F^- incorporation into the MO films likely due to volatile HF elimination during annealing and weak In−F bonding (vide infra).[79] Thus, the annealing time and temperature were optimized to enable MO precursor decomposition, F^- doping, and In−O−In lattice formation in the thin films.

Recently this laboratory has developed a new two-step fast annealing process (Figure 1b)[80] for combustion synthesis, which dramatically reduces the overall processing time versus the conventional one-step process (Figure 1a). This process involves annealing the spin-coated film at a low temperature (120 °C for 1 min) followed by annealing at a higher temperature (250 °C for 1 min; Figure 1b). The first step drives solvent from the as-spun films, thus enhancing the heat generated during combustion synthesis in the second step.[80] Note, increasing the annealing time (i.e., beyond 1 min) and annealing temperature (i.e., beyond 250 °C) does not achieve significant F^- incorporation (Table S2) due to HF elimination by reaction with atmospheric humidity.[79] Annealing under low relative humidity (RH) is not an option, as ambient humidity promotes M-O-M lattice formation and, thus, enhances device performance (Figure S2).[81] Employing this optimized procedure, from 0 to 1.57 atom % fluoride (F:In) can be incorporated in In−O matrices by varying the NH_4F content of the precursor solution from 0 to 50 atom % (Table 1). The

Table 1. Fluoride Incorporation in In−O Thin Films

NH_4F[a] solution concentration	F:In[b] (in solution) [atom %]	F:In[c] (in thin film) [atom %]
0.00 M NH_4F soln	N/A	N/A
0.005 M NH_4F soln	1	no fluorine
0.025 M NH_4F soln	5	0.18 ± 0.15
0.075 M NH_4F soln	15	0.48 ± 0.1
0.15 M NH_4F soln	30	1.27 ± 0.39
0.25 M NH_4F soln	50	1.57 ± 0.26

[a]Precursor solution: Conventional In−O precursor soln (2 mL; see Experimental Section for details) + 7 μL of conc HNO_3 + 200 μL of 0.00/0.005/0.025/0.075/0.15/0.25 M NH_4F soln. [b]As added in solution. N/A indicates not applicable. [c]F1s signals were detected via XPS. F/In ratio calculated by comparing F1s peak with In3d ($In3d_{3/2}$ + $In3d_{5/2}$) peak. Average of four batches. N/A indicates not applicable.

F^- content in the In−O thin films was quantified by XPS (Figure 1c). Note from Table 1 that, when small amounts of NH_4F are added to the precursor solution (e.g., F:In = 1−5 atom %), XPS indicates minimal F^- (F:In = 0.18 atom % max) incorporation in the In−O films. By increasing the NH_4F concentration from 15 to 30 to 50 atom % (F:In), the F^- content in the film increases from 0.48 to 1.27 atom % and then plateaus at 1.57 atom % (F:In), respectively. For the thin-film growth terminology used here, see Table S3. Further increases in precursor solution NH_4F concentration lead to formation of insoluble nanoparticles in the precursor solution. Note that the limited incorporation of F^- from the precursor solution into the amorphous In−O thin film can be understood from the theoretical results: the average F−In bond length is found to be longer in amorphous F:In−O (2.29 Å) than in crystalline InF_3 (2.05 Å), suggesting weaker F−In bonding in amorphous F:In−O. Also, after 1.0 year at room temperature under an N_2 atmosphere, the F:In−O compositions remain unchanged.

From the XPS measurements, the F1s binding energy in all F:In−O thin films is found to be 684.3 ± 0.1 eV (Figure 1c). As the binding energies for typical metal fluorides lie between 683.4 and 686.2 eV, which is far from those of organofluorine compounds (688−689 eV),[82] we can conclude that the F^- incorporated in the In−O matrix is interacting with In. Chemical mapping via XPS also suggests that F^- is homogeneously distributed over the F:In−O surface (Figure 1d) in agreement with computational results (vide infra).

DOI: 10.1021/acs.chemmater.9b04257
Chem. Mater. 2020, 32, 805−820

Thermal Analysis. Thermal analysis of the F:In−O combustion precursors was performed on vacuum-dried samples of the precursor solutions using differential scanning calorimetry (DSC) and thermogravimetric analysis (TGA). All precursors analyzed by DSC exhibit a strong combustion onset exotherm (T_{exo}) at 112.7−164.7 °C, and the corresponding exothermic enthalpy change (ΔH_{exo}) is 439.5−933.4 J/g (Figure 1e). At T_{exo}, an abrupt mass loss occurs in the TGA (Figure 1f), again signifying combustion. A summary of TGA and DSC data can be found in Table 2. Note that the T_{exo} values for all combustion precursors reported here are displaced to significantly lower temperatures (112.7−124.0 °C) versus that of the pristine In−O combustion precursor without added HNO_3 (164.7 °C; Table 2), presumably because HNO_3 addition changes the oxidizer/fuel ratio, altering the combustion process.[83] Furthermore, addition of F^- in the combustion precursor slightly increases T_{exo} by 5.3−11.3 °C compared to that of In−O (Table 2). In contrast, the ΔH_{exo} of the F:In−O samples varies less regularly than those of the In−O samples (Table 2).

Table 2. Summary of DSC Combustion Data

material	T_{exo}[a] [°C]	ΔH_{exo}[a] [J/g]
In−O (w/o HNO_3)	164.7 ± 0.8	802.4 ± 8.9
In−O (with HNO_3)	112.7 ± 2.6	781.1 ± 35.2
0.18 atom % F:In−O	118.0 ± 2.5	759.9 ± 97.9
0.48 atom % F:In−O	118.0 ± 3.2	933.4 ± 64.3
1.27 atom % F:In−O	121.3 ± 3.6	728.0 ± 81.8
1.57 atom % F:In−O	124.0 ± 3.1	439.5 ± 8.4

[a]Average of 2−4 samples.

Thin-Film Morphology and Microstructure. AFM was employed to investigate the surface morphology of the F:In−O films and reveals that the 0.18−1.27 atom % F:In−O films are atomically smooth and have a root-mean-square (RMS) roughness (R_q) of ∼0.141−0.158 nm (Figures 2a and S3). These results are also consistent with widely reported smooth surfaces of combustion-synthesized amorphous MO films.[2,20,57−59,63,66] However, the films having greater F^- content (e.g., 1.57 atom % F:In−O) are slightly rougher (R_q = 0.406 nm) presumably due to in situ formation of aforementioned insoluble nanoparticles in the precursor solution (Figures 2a and S3).

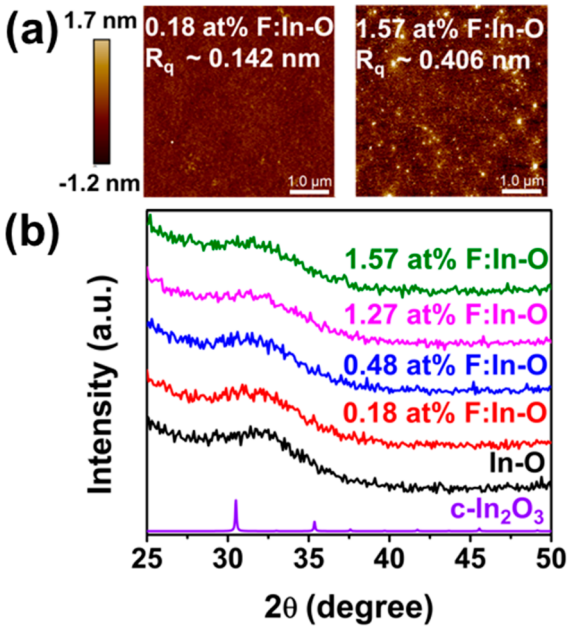

Figure 2. Indicated x atom % F:In−O thin films: (a) AFM height images and RMS roughnesses (R_q), (b) GIXRD patterns.

GIXRD (Figure 2b) data confirm that, under the current fabrication conditions, all the F:In−O films, including the undoped In−O samples, are amorphous. This result contrasts with conventional combustion synthesis of In−O, which evidences crystallization at temperatures as low as 200 °C (annealing time = 30 min).[16] This outcome is in agreement with a recent improvement in combustion processing,[80] in which the current two-step fast annealing process anneals each thin-film layer for only 2 min/layer versus 20−60 min/layer in the conventional one-step combustion synthesis, thus reducing the annealing time so that there is insufficient time for full In−O crystallization. Also, note that differences in stability observed here (with respect to crystallization) between PVD and combustion-synthesized films are consistent with the literature.[84] Furthermore, after 1.0 year at room temperature under an N_2 atmosphere, the F:In−O films remain macroscopically amorphous with no change in composition.

Details of F:In−O film thickness, electron density, and vertical composition variations were next investigated by XRR. Film thickness can be accurately determined by calculating the first derivative of the electron density profile. To calculate the average electron density, the electron density over the area of interest (each layer/entire film) was integrated, and the slope of the linear integrated electron density function was extracted.[40] Table S4 and Figures 3a and S4 report thickness, reflectivity, and density profiles of the present F:In−O thin films. With increase of the F^- content, a slight thickness contraction (1−4%) is observed for most of the F:In−O films, 10.47−10.96 nm, compared to 10.91 nm for In−O (Table S4 and Figure 3a). Note that the average electron density of the In−O films reported here is 1.51 e/Å^3 (Table S4 and Figure 3a), which is somewhat lower than that of combustion-synthesized In−O thin films reported previously (1.7 e/Å^3).[85] This result can be explained by the fact that the In−O films reported here are annealed at far lower temperatures and for shorter times (Figure 1b) compared to standard combustion conditions of 300 °C/20 min/MO layer, Figure 1a.[85] Note that, as the F^- concentration increases from 0 to 0.18 atom %, the average electron density slightly increases from 1.51 to 1.54 e/Å^3. With further F^- incorporation, the average electron density falls monotonically from 1.46 e/Å^3 for 0.48 atom % F:In−O to 1.39 e/Å^3 for 1.57 atom % F:In−O (Table S4 and Figure 3a), possibly reflecting NH_4F decomposition product evaporation. Furthermore, the vertical electron density distribution across the layers for each x atom % F:In−O film (recall that each film is obtained by spin-coating four layers) is more uniform versus the corresponding In−O films (Figure S4), which is similar to the trend observed in boron doping of In−O.[85] Thus, it can be concluded from the XRR experiments that the present F^--doping process yields uniform metal oxide thin films, which is in accord with the computational results (vide infra).

Next, to characterize the MO lattice formation in the combustion-synthesized F:In−O thin films, XPS data were analyzed in the O1s binding region. The spectra can be deconvoluted to reveal three distinct major chemical species:

DOI: 10.1021/acs.chemmater.9b04257
Chem. Mater. 2020, 32, 805−820

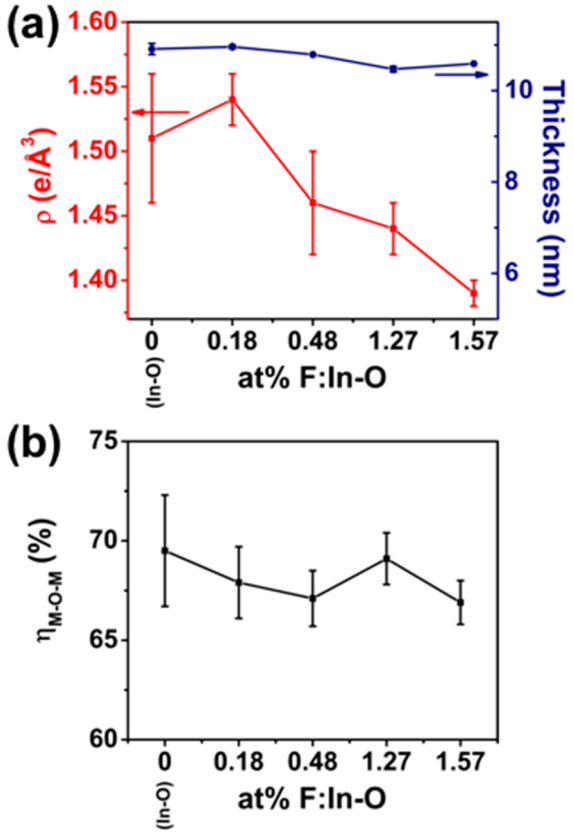

Figure 3. (a) Average electron density (ρ) and average thickness as determined by XRR, (b) ratio of M-O-M peak area to total peak area (η_{M-O-M}) in XPS O1s spectra for the indicated x atom % F:In−O thin films.

(1) metal oxide lattice (M-O-M) at 529.9 ± 0.1 eV, (2) metal hydroxide (M−OH) species at 531.1 ± 0.1 eV, and (3) weakly bound CO_2 and H_2O, species (M-OR) at 532.2 ± 0.1 eV.[20,86] The M-O-M lattice is doubtless the major conduit for charge transport, hence semiconducting properties.[68,87] In contrast, the M−OH and M−OR centers act as charge traps in MO films, thus impeding charge transport.[88] Consequently, M-O-M lattice content defined as the ratio of the M-O-M peak area to the entire O1s peak area (η_{M-O-M}) is a reasonable predictor of efficient charge transport.[20,57] Table S5 and Figures 3b and S5 show the M-O-M, M−OH, and M−OR content in the present F:In−O films, which have high η_{M-O-M} metrics, 66.9−69.1%, which are close to that in In−O (69.5%), signifying good precursor conversion into high-quality MO films. Again note that these values are lower than that achieved for the conventional combustion-synthesized In−O thin films (~70%), reflecting the lower processing temperature used here (Figure 1a,b).[85] Furthermore, F^- addition does not significantly affect M-O-M lattice formation, presumably due to low F^- incorporation (0.18−1.57 atom %) resulting in little disruption of the M-O-M lattice.

Thin-Film Transistor Measurements. The charge-transport properties of F:In−O thin films were evaluated in a bottom-gate top-contact TFT architecture. F:In−O films were deposited on p^{++} -Si/300 nm SiO_2 wafers serving as the gate contact and the gate dielectric, respectively, and aluminum was thermally evaporated through a shadow mask to create source and drain electrodes with a channel length (L) of 100 μm and width (W) of 1000 μm (Figure S6). Representative transfer curves, output plots, and leakage current are shown in Figures 4a,b and S7a−c. Note that the output curves show clear saturation behavior (Figures 4b and S7b). TFT performance is summarized in Table 3 and Figure 4c,d. Postannealing of the devices was not possible for F:In−O even at relatively low

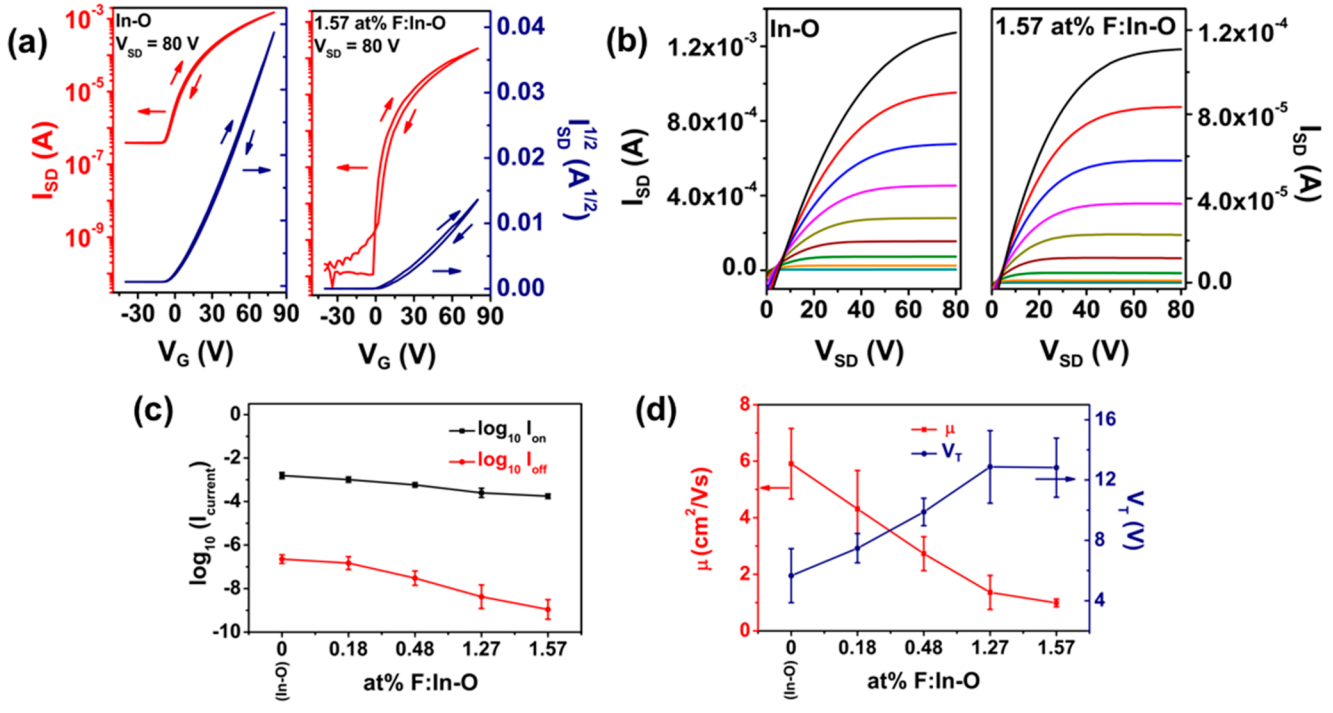

Figure 4. (a) Transfer characteristics, (b) output characteristics (V_G = 0−80 V, 10 V intervals), (c) off-current (I_{off}), on-current (I_{on}), and (d) mobility (μ), threshold voltage (V_T) of the indicated x atom % F:In−O TFTs. (I_{SD} = source-drain current, V_G = gate voltage, V_{SD} = source-drain voltage).

DOI: 10.1021/acs.chemmater.9b04257
Chem. Mater. 2020, 32, 805−820

Table 3. TFT Device Performance of the Indicated *x* atom % F:In−O Thin Films

material	I_{on}[a] [A]	I_{off}[a] [A]	I_{on}/I_{off}	V_T[a] [V]	μ[a] [cm^2 V^{-1} s^{-1}]
In−O	$1.55 \times 10^{-3} \pm 4.99 \times 10^{-4}$	$2.26 \times 10^{-7} \pm 1.02 \times 10^{-7}$	10^3	5.66 ± 1.79	5.91 ± 1.25
0.18 atom % F:In−O	$1.01 \times 10^{-3} \pm 2.85 \times 10^{-4}$	$1.48 \times 10^{-7} \pm 1.01 \times 10^{-7}$	10^3	7.48 ± 0.97	4.31 ± 1.36
0.48 atom % F:In−O	$5.77 \times 10^{-4} \pm 1.37 \times 10^{-4}$	$3.02 \times 10^{-8} \pm 2.30 \times 10^{-8}$	10^4	9.88 ± 0.91	2.73 ± 0.6
1.27 atom % F:In−O	$2.50 \times 10^{-4} \pm 1.20 \times 10^{-4}$	$4.23 \times 10^{-9} \pm 5.27 \times 10^{-9}$	10^4	12.87 ± 2.41	1.36 ± 0.6
1.57 atom % F:In−O	$1.75 \times 10^{-4} \pm 4.18 \times 10^{-5}$	$1.10 \times 10^{-9} \pm 1.14 \times 10^{-9}$	10^5	12.82 ± 1.96	0.99 ± 0.14

[a]Average of more than 10−15 devices (2−3 batches).

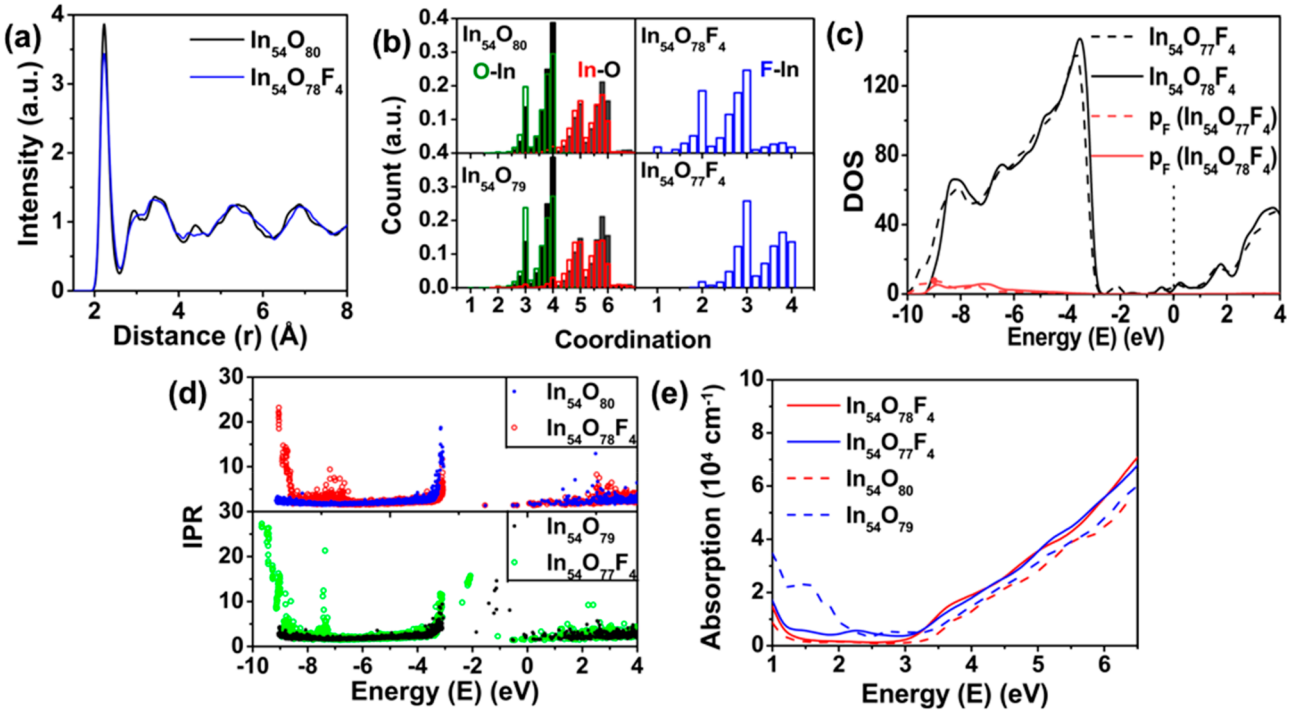

Figure 5. (a) The calculated pair correlation functions for a-$In_{54}O_{80}$ and a-$In_{54}O_{78}F_4$ as obtained from ab initio MD simulations at 300 K. (b) Coordination distribution in a-In−O (solid black bars) and a-F:In−O (open green, red, and blue bars for O, In, and F coordination, respectively) with different oxygen content calculated based on the results of ab initio MD simulations at 300 K over 6 ps time range. (c) Total and partial DOS with contribution from the 2p states of four fluorine atoms (p_F) for a-$In_{54}O_{78}F_4$ (solid line) and a-$In_{54}O_{77}F_4$ (dashed line) as calculated from DFT with HSE potential. The Fermi level is at 0.0 eV. (d) The HSE-calculated IPR for a-$In_{54}O_{78}F_4$ and a-$In_{54}O_{77}F_4$ and for the corresponding a-In−O structures. (e) Optical absorption for non-stoichiometric a-In−O and a-F:In−O as obtained from HSE calculations.

temperature, as the F^-content rapidly declines, unlike typical oxide films (Figure S8).[89,90] Also annealing/postannealing under N_2 (lower O_2 partial pressure) would alter the baseline In−O electronic properties,[91,92] and a major objective of this work is to elucidate effect of F^- doping in In−O. Enhanced switching behavior might be obtained by patterning the channel material; however, conventional AZ lithography degrades the F:In−O films. It is evident from Table 3 and Figure 4 that F^- doping greatly influences the In−O TFT performance. Note that, under the above-mentioned fabrication conditions (Figure 1b), the In−O control TFTs exhibit similar $I_{on}/I_{off} \approx 10^3$, a positively shifted threshold voltage (+5.66 V), and a lower mobility (5.91 cm^2 V^{-1} s^{-1}) compared to conventional combustion-synthesized In−O devices ($I_{on}/I_{off} \approx 10^3$, $\mu \approx 13$ cm^2 V^{-1} s^{-1}, $V_T \approx -12$ V) due to the present lower processing temperature/time.[85] Figure 4c indicates that, as the F^- concentration increases, I_{off} monotonically falls from 2.26×10^{-7} A for In−O to 1.10×10^{-9} A for 1.57 atom % F:In−O. This trend can be explained by the fact that the weakly localized defects in undoped a-In−O may allow current leakage even without a large applied voltage, simply from thermal excitation. F^- doping serves to reduce the leakage by creating deeper defects that are less susceptible to thermal excitation. The TFT on-current (I_{on}) follows the same trend from 1.55×10^{-3} A for In−O to 2.50×10^{-4} for 1.27 atom % F and, finally, falls to 1.75×10^{-4} A for 1.57 atom % F:In−O (Figure 4c). Thus, F^- doping greatly enhances the I_{on}/I_{off} ratio of F:In−O TFTs from 1×10^3 for In−O and 0.18 atom % F:In−O, gradually increasing to 1×10^4 for 0.48 and 1.27 atom % F:In−O, and plateauing at $\sim 10^5$ as in 1.57 atom % F:In−O (Table 3), thus improving the switching properties of In−O TFTs. Simultaneously, as shown in Figure 4d, as more F^- is incorporated in the In−O matrix, the saturation mobility gradually declines from 5.91 cm^2 V^{-1} s^{-1} for In−O to 1.36 cm^2 V^{-1} s^{-1} for 1.27 atom % F and finally drops to 0.99 cm^2 V^{-1} s^{-1} for 1.57 atom % F:In−O, presumably reflecting disrupted octahedrally coordinated In atoms that facilitate electron mobility along low-dimensional In−O_6 chains[38] as well as electron scattering near the loosely bound F^- anions. Note that saturation mobility data are preferred over linear mobility for reporting TFT data, as it does not require threshold voltage data and is less sensitive to contact resistance, thus providing

DOI: 10.1021/acs.chemmater.9b04257
Chem. Mater. 2020, 32, 805−820

Table 4. Experimental EXAFS Fitting[a] and MD Simulation Results[b]

	N		$\sigma^2 \times 10^4$ (Å^2)			ECN		$\sigma^2 \times 10^4$ (Å^2)	
material	1st shell	2nd shell	1st shell	2nd shell	simulation	1st shell	2nd shell[c]	1st shell	2nd shell[c]
c-In_2O_3 powder	6	6	55	45	c-$In_{32}O_{48}$	5.8	5.9	51	43
In−O[d]	5.92 ± 0.25	3.64 ± 0.82	81	122	a-$In_{54}O_{80}$[e]	5.3	3.5	92	116
9.2 atom % F:In−O[d]	5.90 ± 0.29	3.51 ± 0.30	84	126	a-$In_{54}O_{78}F_4$	5.2	3.1	107	145

[a]ΔE = 6.0 eV (In−O) and 3.6 eV (9.2 atom % F:In−O). FOM (*R* factor) = 0.0064 (In−O) and 0.0068 (9.2 atom % F:In−O). [b]Experimental EXAFS fitting results of indicated samples compared with room temperature MD simulation. *N* = coordination number, σ^2 = average variance of bond distance, ECN = effective coordination number. [c]Edge-shared In−In only, excludes face- and corner-shared with similar In−In distances. [d]Average of total 12 scans over two different substrates. [e]Average of total 10 separate MD liquid-quench simulations.

more reproducible and comparable mobility data.[19] Hall mobility measurements could in principle provide ancillary information about bulk transport. However, the electronic structure computations are consistent with the charge transport seen in TFTs; thus, fundamentally, the addition of Hall effect measurement would not change the picture of how F^- doping operates in amorphous In−O films. Note also that, with addition of F^-, the threshold voltages (V_T) of the F:In−O films shift positively from +5.66 V for In−O to +9.88 for 0.48 atom % F:In−O and, then, plateau at ca. +12.87 to +12.82 V for 1.27−1.57 atom % F:In−O, respectively (Figure 4d and Table 3). Furthermore, note that the TFT subthreshold swing (SS) and interfacial charge density (N_{it}) decrease considerably with increasing F^- content, approaching those of other solution-processed oxides (Figure S9 and Table S6).[93,94] Also, *I*−*V* hysteresis of the transfer curves (Figures 4a and S7a) indicate very low charge trapping.[95]

Finally, the F:In−O TFTs were next subjected to a V_G−V_{SD} constant bias of +20 V for 200 s intervals over 1200 s to test for bias stability (Figure S10). These bias stress results indicate that F^- doping increases the TFT positive bias stability, especially after 200 s (first cycle) due to formation of deeper, localized trap states inside the band gap as compared to undoped In−O, as indicated by computational results (Figure 5d).

Computational Modeling and Electronic Structure of F:In−O. To shed light on the role of F^- in the structural, optoelectronic, and charge-transport properties of F:In−O thin films, ab initio molecular dynamics simulations and accurate density function theory calculations were performed for amorphous $In_{54}O_{80}$, $In_{54}O_{79}$, $In_{54}O_{78}F_4$, and $In_{54}O_{77}F_4$ structures with different [M]/[O] ratios to analyze the role of F^- doping in defect formation. Note that the F^- concentration in the theoretical model is 7.41 atom % (F/In = 4:54), which is higher than that of the experimental F/In ratios (0.18−1.57 atom %). While simulations of larger than the 135-atom amorphous supercell using ab initio MD and DFT−Heyd-Scuseria-Ernzerhof (HSE) approaches are beyond the current capabilities of state-of-the-art supercomputers, the smallest possible F concentration (F/In = 1:54) would not provide statistically reliable results regarding the structural preferences of the F^- in the modeled oxide supercells as well as its effect on the properties of the In−O host.

First, to understand the effect of F^- doping on the local and medium-range structure, the average pair correlation functions $g(r)$ were computed for a-In−O and a-F:In−O (Figure 5a). The first-shell peak corresponding to the nearest In−O bonds is clearly defined; at longer range, the structural features are suppressed. Upon F^- introduction in the In−O system, the height of the first peak decreases, which signifies stronger local distortions in F:In−O versus In−O. Indeed, the calculated average variance of bond distances (σ^2) in the first-shell In−O distances increases from $\sigma^2 = 9.2 \times 10^{-3}$ Å^2 (9.4×10^{-3} Å^2) in $In_{54}O_{80}$ ($In_{54}O_{79}$) to 1.07×10^{-2} Å^2 (1.13×10^{-2} Å^2) in $In_{54}O_{78}F_4$ ($In_{54}O_{77}F_4$) (Table 4). Note that the obtained local distortions in the In−O_X polyhedra in F:In−O with the small concentrations of F^- (5 atom % of fractional anion substitution) are similar to those calculated for amorphous In−Ga−O and In−Zn−O with as large as 20% fractional cation substitution,[38,39,96] indicating the effectiveness of F^- to enhance the local disorder in a-In−O matrices.

Next, the role of F^- doping on coordination of In and O atoms was investigated by calculating the effective coordination number (ECN) distribution in In−O and F:In−O at 300 K over a 6 ps time range as shown in Figure 5b. Comparing the structures without (w/o) and with F^-, namely, $In_{54}O_{80}$ and $In_{54}O_{78}F_4$, the average coordination is slightly reduced from 5.3 to 5.2 for the In atoms (Table 4) and from 3.6 to 3.5 for O atoms upon F^- incorporation. Accordingly, the average In (O) coordination is reduced from 5.2 to 5.1 (from 3.6 to 3.4) for the oxygen-deficient structures $In_{54}O_{79}$ and $In_{54}O_{77}F_4$, respectively. Thus, similar to an additional cation in a-In−O, for example, In−Sn−O, In−Zn−O, In−Ga−O, etc.,[38,39] addition of F suppresses the number of fully coordinated In atoms (with the effective coordination of 5.5 and above) that serve as nucleation sites during crystallization. Fluorine itself is two-, three-, or four-coordinated to In atoms, and the F coordination is highly sensitive to the O stoichiometry (Figure 5b). Specifically, the F atoms tend to have higher coordination in the structure with lower O content: the average coordination of F atoms increases from 2.5 in $In_{54}O_{78}F_4$ (the average In−F distance is 2.29 Å) to 3.2 in $In_{54}O_{77}F_4$ (the average In−F distance is 2.26 Å), that is, F adjusts its coordination to compensate the lack of O in the structure. Note that the number of twofold-coordinated F atoms is fully suppressed in $In_{54}O_{77}F_4$, despite the fact that the F atoms are two-coordinated with In atoms (having the In−F distance of 2.05 Å) in hexagonal indium fluoride (InF_3) structure. Thus, the above results suggest that (i) the longer In−F distances in F:In−O as compared to crystalline InF_3 point to much weaker In−F bonds in the former and (ii) the strong sensitivity of the F coordination to the O content (O stoichiometry) is expected to play an important role in defect formation, carrier transport, and optical properties. Finally, no F^- clustering is observed in our models—in accord with the uniform distribution of F^- in experimental observations (Figure 1d).

While the effect of F^- doping on the average In−O (first-shell) coordination is weak, as demonstrated by both the theoretical and EXAFS data (Table 4), F reduces the number of edge-shared In−O polyhedra in the second shell from 3.5 in $In_{54}O_{80}$ to 3.1 in $In_{54}O_{78}F_4$, thus promoting the medium-range disorder (Table 4). The changes in the second-shell

DOI: 10.1021/acs.chemmater.9b04257
Chem. Mater. 2020, 32, 805−820

coordination arise from a "ripple" effect, when the In−O bond distances fluctuate within a given In−O_x polyhedron and are further corroborated by the EXAFS studies (Table 4). At room temperature, the effective coordination variance, calculated based on the atomic configurations from 3000 MD steps (time period of 6 ps), increases from 0.15 and 0.14 in $In_{54}O_{80}$ and $In_{54}O_{79}$ to 0.17 and 0.16 for $In_{54}O_{78}F_4$ and $In_{54}O_{77}F_4$, respectively (Figure S11). The values for a-F:In−O are notably higher as compared to the amorphous structures with cation substitution, namely, 0.14 in a-IGO or a-IZO and 0.15 in a-ITO[38] obtained for large fractional X = Ga, Zn, or Sn substitution of ∼20% (ratio X/In = 5:22) suggesting the high efficiency of F^- to frustrate the lattice. Importantly, the calculated average coordination variance of F atoms in $In_{54}O_{78}F_4$ at room temperature is 0.27, which is 3 times higher than that for O atoms (0.10) and also considerably higher than the average variance of extra cations incorporated in a-In−O, that is, 0.07 for Ga atoms, 0.06 for Sn, and 0.11 for Zn.[38] This finding suggests that, in marked contrast to additional cations, which were shown to assume and maintain their preferred coordination, owing to the stronger metal-O bonding as compared to that of In−O,[38,69,96] the incorporated F atoms are bonded weakly to the neighboring In atoms (as supported by the calculated electronic properties, see below). We note that the F coordination variance decreases to 0.16 in $In_{54}O_{77}F_4$, Figure S11, suggesting that F compensates the lack of oxygen and contributes to a more uniform charge distribution in this ionic compound by increasing and stabilizing its coordination. In this case, F remains to be loosely bound to the neighboring In atoms, since the average In−F distance in $In_{54}O_{77}F_4$ (2.26 Å) is much longer than that in crystalline InF_3 (2.05 Å).

The electronic properties of In−O and F:In−O were calculated using a hybrid functional approach (HSE) for an accurate description of the band gap and optical properties. Figure 5c illustrates the total density of states (DOS) for $In_{54}O_{78}F_4$ and $In_{54}O_{77}F_4$. The calculated partial DOS reveals that the 2p states of fluorine atoms are located deep in the valence band, from −9 to −7 eV, or ∼6 eV below the bottom of the conduction band (Figure 5c). This energy value corresponds closely to our HSE-calculated band gap in crystalline InF_3, namely, 6.5 eV, pointing out that the interaction between the F2p and In5s states is similar in c-InF_3 and a-F:In−O. In the latter, however, the F-states are strongly localized, as expected for a weakly interacting impurity (Figure 5d), and are distinct in energy owing to the coordination differences of the F atoms. Specifically, the states of the lower-coordinated F atom (ECN ≈ 1.6) contribute at higher energy (−6.7 eV), whereas those of the high-coordinated F atom (ECN ≈ 3.3) are deeper (−9 eV). Accordingly, the F states in $In_{54}O_{77}F_4$ are located even deeper—given the higher F coordination in this case (Figure 5b).

Because the F-states do not contribute to the DOS in the vicinity of the Fermi level, addition of F does not appear to have a direct effect on the number of carriers and their mobility. Indeed, a comparison of the calculated inverse participation ratio (IPR) for $In_{54}O_{80}$ and $In_{54}O_{78}F_4$, as in Figure 5d(upper), shows similar delocalized character for the states near the Fermi level, as separately confirmed by the charge density distribution and Bader charge analysis. Nevertheless, the presence of F affects the local and medium-range structure of the In−O host (Table 4). We believe that the observed decrease in the carrier mobility with F incorporation can be explained by (i) the reduced number of octahedrally coordinated In atoms and, hence, lower probability of the formation of low-dimensional In−O_6 chains that have been shown to promote carrier mobility[38] and (ii) increased atomic vibrations near F atoms associated with the large coordination variance (Figure S11) that leads to a stronger free electron scattering.

Furthermore, we investigated the role of F^- doping on the electronic properties of deep electron traps by comparing the calculated IPR plots for the structures with lower O content, $In_{54}O_{79}$ and $In_{54}O_{77}F_4$ (Figure 5d(lower)). In the latter case, the electron trap state is ∼1 eV deeper and more localized in energy as compared to the undoped In−O, where the defect states are shallower and less localized. To quantify the electron localization, we performed Bader analysis of the calculated charge density distribution for these defect states.The results show that the Voronoi volume in which the integrated charge density is equal to one (trapped) electron in a-F:In−O is equal to only 2% of the supercell, whereas the single trapped electron in a-In−O is localized within 11% of the total cell volume, Figure S12. Further analysis of the electronic and structural characteristics of the atoms with the highest contributions to the defect charge density shows that the antibonding states of the O atoms that are the nearest neighbors for the two most under-coordinated In atoms (ECN = 2.93 and 3.86 in $In_{54}O_{79}$ and 2.96 and 4.60 in $In_{54}O_{77}F_4$), have nearly 7 times larger contributions to the Bader charge as compared to all other O atoms located further away from the defect. In contrast, the contributions from an F atom that is also a nearest neighbor of one of the under-coordinated In atoms in $In_{54}O_{77}F_4$ is 7 times smaller—in accord with the finding that the F antibonding states do not contribute to the conduction band near the Fermi level and thus are unavailable for the trapped electron.

More importantly, the presence of F^- results in a larger number of under-coordinated In atoms (Figure 5b) and suppressed polyhedra sharing (Table 4). As a result the distance between the two most under-coordinated In atoms is much shorter in $In_{54}O_{77}F_4$ (2.75 Å) than in $In_{54}O_{79}$ (3.1 Å), leading to a stronger In−In metallic bond and, hence, stronger localization of the deep trap. While the formation of deeper defects limits the number of free carriers (in both F^--doped and undoped a-In−O), F^- doping may (i) reduce the off-current leakage by decreasing the number of weakly localized defects that can be thermally excited and (ii) promote better transistor stability by making it more difficult for the trapped electron to escape into the conduction band under applied voltage. This finding is similar to recent results for a-In−O doped with small concentrations of boron that leads to stronger localized deep traps.[85]

Finally, the calculated optical absorption illustrates the role of F^- doping on the optical transmission within the IR and visible range (Figure 5e). Most importantly, the strong localization of the deep trap defects in a-F:In−O results in a smaller overall absorption within the near-IR/visible range—in contrast to undoped In−O, where the defect, being spread in energy (Figure 5d), causes significant absorption within 1.4−2.2 eV (Figure 5e). This peak is suppressed in F^--doped oxide, in accord with the more energetically localized state at ∼2.5 eV below the Fermi level in IPR (cf. Figure 5d(lower)). The absorption at 2.5 eV in this case is small, since the intensity of the electron transitions at this energy is suppressed, owing to the more localized nature of the defect state. The calculated

DOI: 10.1021/acs.chemmater.9b04257
Chem. Mater. 2020, 32, 805−820

optical band gap of the a-$In_{54}O_{78}F_4$ is ~2.9 eV, which is somewhat smaller than that calculated for a-In−O, 3.2 eV. The theoretical results suggest that the presence of F2p-states effectively shifts the top of the valence band to a higher energy (Figure 5d) and slightly reduces the dispersion of the conduction band, resulting in a smaller band gap. Experimentally, the optical spectra of F:In−O and In−O films having the same thickness (10 nm) and preparation method as those for TFT fabrication (~1.57 atom % F) were measured. Note, this F^- content is somewhat lower than that used in the computations. From the data in Figure S13 and Table S7, the measured bandgap of In−O is 3.23 ± 0.11 eV compared to 3.29 ± 0.07 eV for 1.57 atom % F:In−O. Considering the accuracy of the Tauc method, these values are statistically indistinguishable and imply that F^- doping has only a small effect on the amorphous In−O bonding, which in turn determines the fundamental band gap in the oxides—as, indeed, observed from the present EXAFS measurements and MD simulations, Table 4. Note also that the present In−O Tauc plot is almost identical to a low-temperature solution-processed In−O film reported in the literature (Figure S13).[97] Finally, increased absorption within 2−4 eV indicates increased disorder in amorphous F:In−O,[38] which is again consistent with our EXAFS and MD data.

Microstructure Analysis of F:In−O Versus In−O. Encouraged by the computational results and to gain experimental insight into the microstructural changes in the In−O_x polyhedra due to F^- incorporation, extended X-ray absorption fine structure analysis of a-In−O and a-F:In−O thin films was performed. Measurements were recorded at the In K-edge (27940 eV) on ~52−70 nm thick amorphous thin films of undoped In−O and 9.2 atom % F^--doped In−O films (9.2 atom % F:In−O) ($\eta_{M\text{-}O\text{-}M} \approx 66\%$). Note that thicker samples (~52 nm for 9.2 atom % F:In−O and ~70 nm for In−O) were prepared (see Experimental Section for further details) for EXAFS study to incorporate an adequate amount of F^- in In−O matrices, so that F/In ratios of EXAFS and theoretical model (7.41 atom %) studies are close to capture F^--induced structural relaxation (Figure S14). Qualitative EXAFS data analysis focused on the first two shells, and details of EXAFS analysis can be found in Figures 6 and S15 and Tables 4 and S8. The strong peak at $R < 2$ Å corresponds to the In−O shell, while the two peaks evident at $2 < R$, Å < 4 correspond to two In−In shells of different configurations (Figure 6a).[39,40] A small peak due to the second shell is apparent in the pseudo-radial distribution functions (p-RDFs) of the amorphous In−O and 9.2 atom % F:In−O films, while the third shell is completely suppressed (Figure 6a), confirming the amorphicity of these samples.[39,40]

The coordination numbers (N) of the first two shells of c-In_2O_3 powder are 6. As shown in Table 4 and Figure 6b, both undoped In−O (N = 5.92) and 9.2 atom % F:In−O (N = 5.90) films exhibit under-coordination compared to c-In_2O_3, which is consistent with previous reports.[39,40] Coordination of the first shell remains largely unchanged by incorporation of F^-. However, coordination of the second shell shows a decrease upon F^- doping (Table 4 and Figure 6b). Concomitantly, the variances of bond distances (σ^2), which are used to quantify the thermal and structural disorders of metal oxide matrices,[39] for both the first- and second-shell interactions, are appreciably increased (Table 4 and Figure 6b). The computational results (Table 4) are consistent with these findings. Therefore, F^- doping increases the amorphous

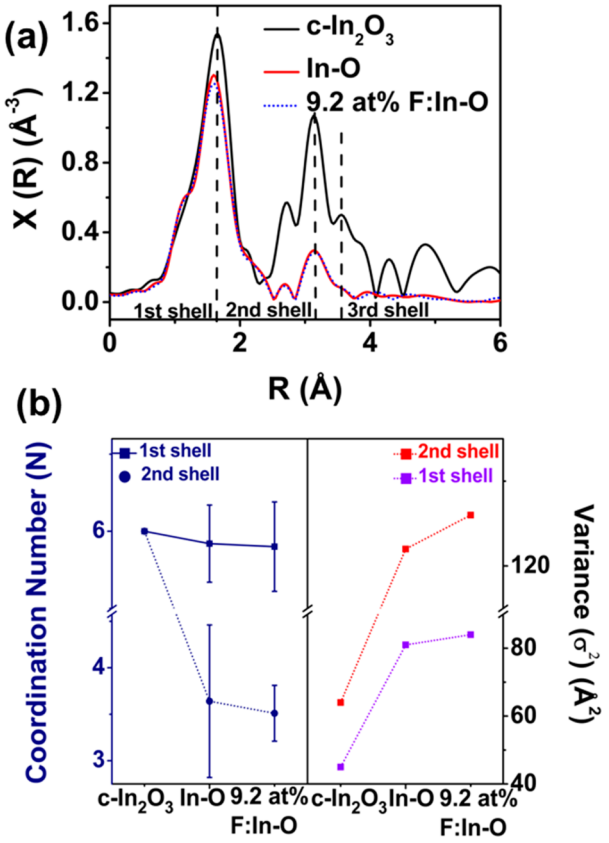

Figure 6. (a) Comparison of the EXAFS-derived In K-edge p-RDFs and (b) EXAFS-derived coordination number (N), average variance of bond distance (σ^2) of c-In_2O_3 powder, amorphous In−O thin film (~70 nm), and amorphous 9.2 atom % F:In−O thin films (~52 nm).

character of these films. The above finding has also been observed in both poly(vinylpyrrolidone) (PVP)-doped and poly(ethylenimine) (PEI)-doped In−O thin films.[40,41] This result is also consistent with the TFT mobility trends versus the F^- content (Table 3), indicating that F^- disrupts lattice and electron conduction pathways, thus reducing mobility. Thus, our result is consistent with the literature trend, ubiquitous across cation-doped (e.g., Ga^{3+}, B^{3+}, Y^{3+}, etc.)[20,39,85] and polymer-doped (PEI, poly(vinyl alcohol) (PVA), PVP)[40,41] metal oxides, that increased amorphicity leads to a decrease in mobility due to disruption of M-O-M lattice, further solidifying the present TFT data.

Finally, the MD simulations predict the first-shell coordination of 5.3 and 5.2 for undoped In−O and 7.4 atom % F:In−O, respectively, which is lower than the observed first-shell coordination number in both films (Table 4). The discrepancy is likely to be due to the different O stoichiometry in the combustion-synthesized films and in the modeled structures. While the effect of F^- doping on the first-shell coordination is weak, both the experimental and theoretical data show that F^- doping suppresses the second-shell coordination, that is, the number of edge-shared In−O polyhedral, and enhances structural disorder (σ^2) at medium range (Table 4).

Comparison with the Literature. As discussed above, MD + DFT computations provide support for the experimental reduction of charge-transport efficiency in amorphous F:In−O, as the F^- content increases as the result of reduced octahedral In−O_6 connectivity and enhanced electron scattering (vide supra). This result may appear to be

DOI: 10.1021/acs.chemmater.9b04257
Chem. Mater. 2020, 32, 805−820

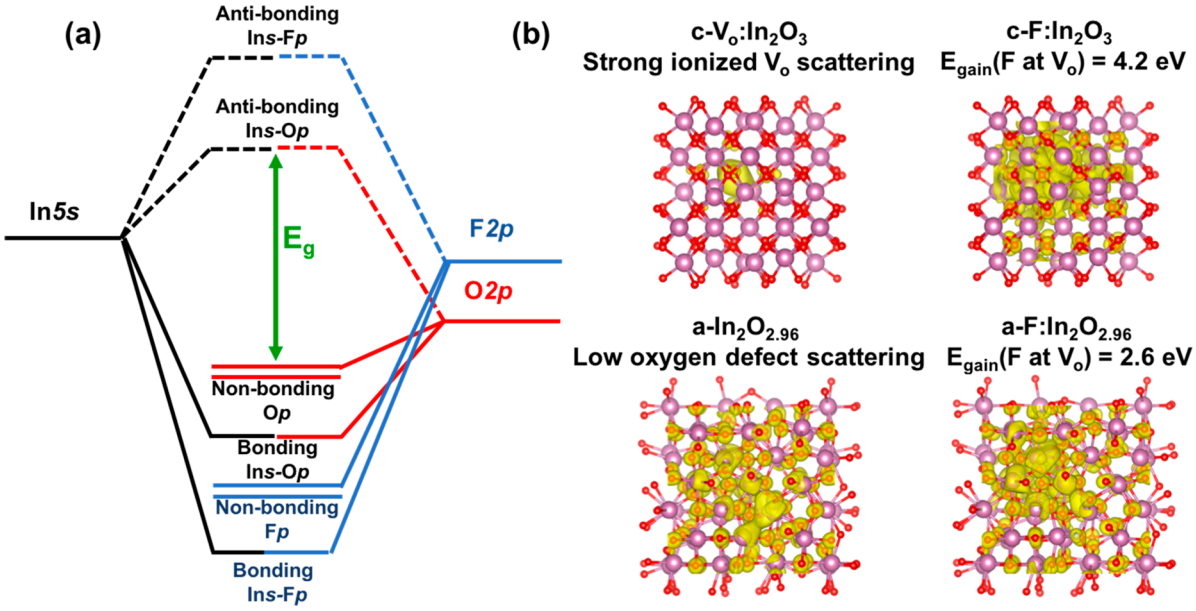

Figure 7. (a) Molecular orbital depiction of hybridization of In5s, F2p, and O2p orbitals in crystalline and amorphous F:In−O. (b) Calculated conduction band charge density near defects in indicated crystalline and amorphous indium oxides. (top left) Crystalline In_2O_3 with oxygen vacancies (c-V_O:In_2O_3), (top-right) crystalline F^--doped In_2O_3 (c-F:In_2O_3), (bottom-left) amorphous $In_2O_{2.96}$ (a-$In_2O_{2.96}$), (bottom-right) amorphous F^--doped $In_2O_{2.96}$ (a-F:$In_2O_{2.96}$).

in contrast with TFT/transport data reported in the Introduction,[47−51,53−56] where F^- doping was found to enhance transport characteristics. Thus, it is important to clarify this aspect. Fluoride (F^-) is an excellent n-type dopant in crystalline oxides, when it substitutes oxygen (O), providing one free carrier (e^-) per substitution based on eq 1.

$$O_o^X + \frac{1}{2}F_2 \rightarrow F_o^{\cdot} + \frac{1}{2}O_2 + e' \quad (1)$$

Thus, *for any crystal domains,* F^- will act as a donor in conducting (e.g., FTO[72−78]) or semiconducting (e.g., F:ZnO[55]) metal oxides. Because the F states do not contribute near the band edges (Figure 7a), due to the greater In−F bond strength (516 kJ/mol) versus the In−O (346 kJ/mol),[98] the presence of F^- cannot contribute to the free electron scattering—as an O vacancy in the crystalline oxide does. Moreover, F^- doping of crystalline In_2O_3 is likely to result in fluorine occupying the O vacancy site, reducing the free electron scattering on ionized O vacancies. Indeed, from additional calculations we find that the energy gain when a F atom is placed at an O vacancy site in *crystalline* In_2O_3 and the structure is relaxed is as large as 4.2 eV. The resulting electronic structure corresponds to degenerate doping with a pronounced Burstein−Moss shift of 1.2 eV. Although not strictly comparable to present work due to differences in sampling (pressed pellet vs thin films), phase differences, crystallinity, and transport measurement technique, work by Mori et al. provides similar insights regarding InOF versus In_2O_3.[43] Thus, both the carrier concentration and the mobility are expected to increase in F^--doped (poly)crystalline MOs.

The transport properties in amorphous films such as the present are primarily governed by the nanostructure, strain, and atomic vibrations,[38] whereas ionized impurity scattering plays a less significant role. This is because any defect in amorphous oxide is effectively screened due to a strong structural relaxation, which affects atoms well beyond the nearest neighbors of the defect—in contrast to a crystalline material with limited degrees of freedom.[38] Such a screened oxygen defect is less attractive for F^- in amorphous F:In−O.

Our calculated energy gain in amorphous indium oxide with an F atom placed between the two under-coordinated under-shared In atoms (the latter represents an oxygen "vacancy" in amorphous oxides[38]) and upon structural relaxation, is only 2.6 eV, significantly smaller than that in crystalline In_2O_3 (4.2 eV). The calculated electronic structure reveals that addition of F^- results in charge redistribution, Figure 7b, and reduction of the Burstein−Moss shift from 1.5 eV (oxygen deficient amorphous oxide) to 1.2 eV (F^--doped amorphous oxide).

Because the incorporated F^- assumes its preferred local structure in the amorphous In−O matrix (vide supra) as also observed in cation-doped amorphous In−O,[38,39] oxygen defects remain primary donors of free carriers in multi-component amorphous oxides. Thus, in amorphous films, the presence of F^- does not enhance carrier generation and reduces the mobility by disrupting the In−O—In lattice, leading to increased disorder, and also due to electron scattering near the loosely bound F^- ions (vide supra).

Direct correlation of the results here with those of previous studies is not straightforward in all cases, since several studies do not discuss the degree of film crystallinity after F^- incorporation in any detail and upon long postfilm deposition annealing treatments (typically ∼350 °C for 20 min to 3 h). Thus, there is limited/no information on the local structure of most F^--doped metal oxides.[47−51,53−56] Note that "X-ray diffraction amorphous" metal oxide thin films may still contain nanocrystals for deposition temperatures as low as −50 °C.[99] Thus, we speculate that F^- doping when nanocrystalline domains are present as in PVD-deposited metal oxide thin films may explain the mobility increase in these films.[47−51] In contrast, the F:In−O thin films synthesized in the present study are prepared by a very low-temperature/short annealing time procedure and are thus reasonably expected to have fewer nanocrystalline inclusions as opposed to long postannealing treatments (350 °C for 20 min to 3 h) reported for some F^--

DOI: 10.1021/acs.chemmater.9b04257
Chem. Mater. 2020, 32, 805−820

doped metal oxides.[47−51] Therefore, a decline in TFT mobility is observed versus the F^- content as expected from the present computational and EXAFS data. We also note that these films cannot be crystallized as in post-deposition annealing studies at relatively low temperature and low humidity, the F^- content rapidly declines (Figure S8), unlike typical combustion-synthesized oxide films.[89,90] Also annealing/postannealing under N_2 (lower O_2 partial pressure) would alter the baseline In−O electronic properties.[91,92]

CONCLUSIONS

This contribution presents the first detailed investigation of F^- doping of an a-MO thin-film semiconductor. Low-temperature combustion synthesis and short annealing times provide a rapid, energy-efficient, and environment-friendly growth process. With F:In−O thin films having varied F^- concentrations, a detailed thin-film organization/electronic structure study was performed. XPS reveals that F^- is homogeneously distributed throughout the films and ionically bound to In. AFM, GIXRD, and XRR studies confirm smooth, dense, amorphous F:In−O films, which should be compatible with flexible substrates. TFTs reveal that increasing F^- content correlates with decreasing I_{off} and I_{on} as well as an increasing I_{on}/I_{off} ratio, thus affording superior switching properties versus In−O-based TFTs. The effects of F^- doping on the local and medium-range structure, trap states, and charge-transport properties of these films were thoroughly investigated with ab initio MD simulations and DFT calculations and corroborating EXAFS analysis. These results reveal that F^- doping inhibits crystallization by enhancing the local and medium-range disorders and increases the atomic motion, which has a negative effect on the carrier mobility. At the same time, F^- likely enables the formation of deep, localized trap states, which help to reduce TFT I_{off} and increase transparency in the near-IR/visible region versus undoped a-In−O. This is the first in-depth study to accurately describe, both through experiment and theory, structure−function relationships in an industry-relevant *amorphous* F^--doped oxide semiconductor, which is significantly different from crystalline F:In−O. Thus, this study should advance our understanding of anion-doped MO thin films achievable via solution-based methods, assisting relevant advances in technology.

EXPERIMENTAL SECTION

Combustion Precursor Solution Preparation. All chemicals were purchased from Sigma-Aldrich and were used without further purification.

Precursor Solution Concentration, 0.05 M (for AFM, GIXRD, XRR, XPS, TFT, UV−vis sample preparation). Exactly 354.88 mg of $In(NO_3)3{\cdot}xH_2O$ was dissolved in 20 mL of 2-methoxyethanol before addition of 100 μL of acetylacetone and 45 μL of ammonium hydroxide solution (14.5 M), and the resulting 0.05 M solution was stirred for 12−14 h. In separate high-density polyethylene (HDPE) vials, adequate amounts of NH_4F were dissolved in Milli-Q water to prepare 0.005, 0.025, 0.075, 0.15, and 0.25 M solutions. Approximately 1 h prior to spin coating, 200 μL of Milli-Q water/0.005 M/0.025 M/0.075 M/0.15 M/0.25 M NH_4F solution was added to 2 mL of combustion precursor solution along with 7 μL of conc HNO_3 acid to afford the required F/In ratio. Precursors for thermal analysis were prepared by removing solvent by vacuum drying for 3 d at 25 °C. TGA and DSC were performed using an SDT Q600 instrument under a N_2 flow rate of 70 mL/min and a heating ramp rate of 10 °C/min from 30 to 500 °C.

Precursor Solution Concentration 0.25 M (for EXAFS). Exactly 887.2 mg of $In(NO_3)_3{\cdot}xH_2O$ was dissolved in 10 mL of 2-methoxyethanol before the addition of 250 μL of acetylacetone and 112.5 μL of ammonium hydroxide solution (14.5 M), and the resulting 0.25 M solution was stirred for 12−14 h. In separate HDPE vials, 92.6 mg of NH_4F was dissolved in 2 mL of Milli-Q water. Approximately 1 h prior to spin coating, 500 μL of Milli-Q water/NH_4F solution was added to 5 mL of combustion precursor solution along with 87.5 μL of conc HNO_3 acid to afford the required F/In ratio (0/50 atom %).

Transistor Fabrication and Electrical Characterization. p^{+2}-Si wafers with 300 nm thermally grown SiO_2 were used as the gate electrode and dielectric layer, respectively. Before spin-coating, the substrates were cleaned ultrasonically in a 1:1 mixture of isopropyl alcohol and acetone three times (10 min each), followed by 5 min in an O_2 plasma. Then the filtered precursor solutions (using 0.2 μm syringe PTFE membrane) were spin-coated at 3500 rpm for 30 s and then annealed on a hot plate at 120 °C for 1 min followed by 250 °C for 1 min (relative humidity ∼33−45%). This process was repeated four times to achieve the desired thickness. Finally, 40 nm Al source drain electrodes were thermally evaporated to form a channel length of 100 μm and channel width of 1000 μm. TFT characterization was performed under ambient light and atmosphere on a custom probe station using an Agilent 1500 semiconductor parameter analyzer. Electron mobility (μ) was calculated in the saturation regime using the following equation:

$$I_{SD} = \frac{\mu C W (V_G - V_T)^2}{2L} \tag{2}$$

Here C is the capacitance per unit area of the dielectric layer, V_T is the threshold voltage, V_G is gate voltage, and I_{SD} is the source-drain current. W and L are channel width and length, respectively.

Subthreshold swing (SS) was calculated using the following equation:[3]

$$SS = \frac{dV_G}{d \log_{10} I_{SD}} \tag{3}$$

Interfacial charge density (N_{it}) was calculated using the following equation:[100]

$$SS = \ln 10 \frac{kT}{q}\left(1 + \frac{qN_{it}}{C_i}\right) \tag{4}$$

Here, k is the Boltzmann constant, T is the absolute temperature (T = 298 K here), q is the charge of the carrier (1.602×10^{-19} C), and C_i is capacitance per unit area of the dielectric (for SiO_2, C_i = 11 nF/cm^2).

Oxide Film Characterization. AFM film topographies were imaged with a Bruker Dimension FastScan atomic force microscope using tapping mode.

GIXRD and XRR measurements were performed with a Rigaku SmartLab Thin-film Diffraction Workstation using a high-intensity 9 kW copper rotating anode X-ray source, which is coupled to a multilayer optic. XRR data were fit with the Igor-based MOTOFIT package.

UV−Vis samples were prepared on quartz substrates, and the UV−vis spectra were acquired using a PerkinElmer LAMBDA 1050 UV−vis−NIR spectrophotometer (NIR = near-infrared).

XPS analyses were performed on Thermo Scientific ESCALAB 250Xi at a base pressure of 4.5×10^{-10} mbar. Spectra were obtained after the surface of the film was etched for ∼2 nm to minimize surface contamination.

EXAFS measurements were performed at beamline 5BM-D at the Advanced Photon Source at Argonne National Laboratory. Data were collected in fluorescence mode at the In K-edge (27940 eV) using a PIPS detector. The reference powder was uniformly spread on tape and measured in transmission mode. The normalized linear EXAFS absorption coefficient $\chi(k)$ can be fit by the equation

$$\chi(k) = {S_0}^2 \sum_i \frac{N_i |f_i(k)|}{k {R_i}^2} \sin\left[2R_i k + \frac{2}{3} C_3 k^3 + \varphi_i(k)\right] e^{-2\sigma_i^2 k^2} \tag{5}$$

DOI: 10.1021/acs.chemmater.9b04257
Chem. Mater. 2020, 32, 805−820

where S_0^2 is the intrinsic loss factor, $\lambda(k)$ is the electron mean free path, N_i and R_i are the coordination number and bond distance of the ith shell of the absorbing atom, C_3 accounts for the effect of anharmonicity in the distance distribution, $f_i(k)$ and $\delta(k)$ are the backscattering amplitude and the phase shift, and $e^{-2k^2\sigma_{R_i}^2}$ is the Debye−Waller factor—a measure of the structural disorder or variation in R_i. The Fourier transform of $\chi(k)$ generates a p-RDF for the absorbing atom. We are interested in how the coordination number, bond distances, and Debye−Waller factors vary as a function of fluorine doping. Data reduction and analysis were performed using the Demeter software package.[101] The initial model was obtained using FEFF simulations based on crystalline In_2O_3. The intrinsic loss factor (S_0^2 = 1.01) was determined from the fit to the crystalline reference sample. The data range used in obtaining these results is k = 2.4−12 Å^{-1} and R = 1.0−3.8 Å with a k-weight of 2.

Theoretical Analysis. The amorphous $In_{54}O_{80}$, $In_{54}O_{79}$, $In_{54}O_{78}F_4$, and $In_{54}O_{77}F_4$ structures were obtained using ab initio molecular dynamics liquid-quench approach as implemented in the Vienna Ab Initio Simulation Package (VASP).[102−105] The calculations used DFT[106,107] with periodic boundary conditions and the PBE functional[108,109] within the projector augmented-wave method.[110,111] A bixbyite cell of In_2O_3 with crystalline density of 7.12 g/cm^3 and with 134 atoms per cell was used as initial structure, which was melted at 3000 K to eliminate any crystalline memory. For F:In−O, four F atoms were introduced into the cell, and the number of oxygen atoms was adjusted ($In_{54}O_{78}F_4$) to keep the same anion charge as in undoped indium oxide. The cell density was set to 6.92 g/cm^3, which was calculated based on the fraction of InF_3 having the crystalline density of 4.7 g/cm^3. Note that the concentration of F in the theoretical model is F/In = 4:54, which is somewhat greater than that in the experiments (0.18−1.57 atom %); a smaller F content in the F:In−O supercell would likely be inadequate to capture the structural preferences of the F anion. To model non-stoichiometric structures with lower O content, O atom(s) were randomly removed. All structures had additional melting at 3000 K for 10 ps to randomize the sub-stoichiometric multicomponent configuration and stabilize the total energy. Next, liquid quench simulations were performed as follows. Each structure was cooled to 2500 K at the MD rate of 100 K/ps and then rapidly quenched to 100 at 200 K/ps rate. An energy cutoff of 260 eV and single Γ-point were was used during melting and quenching processes. Finally, each structure was equilibrated at 300 K for 6 ps with a cutoff energy of 400 eV. All MD simulations were performed in the NVT ensemble with the Nose-Hoover thermostat using an integration time step of 2 fs. For an accurate structural analysis of the simulated amorphous oxides, the room-temperature In−O and F:In−O structures were used. The average pair correlation function and the average effective coordination number for first, second, and third shells were calculated according to literature-reported techniques.[96,112,113] The resulting atomic structures were plotted using VESTA software.[114]

Next, the atomic configurations obtained from the ab initio MD simulations were optimized within DFT using the PBE functional. For the optimization, the cutoff energy of 500 eV and the 4 × 4 × 4 Γ-centered k-point were used; the atomic positions were relaxed, until the Hellmann−Feynman force on each atom was below 0.01 eV/Å. The electronic and optical properties of the optimized amorphous In-based oxides were calculated using the hybrid Heyd-Scuseria-Ernzerhof (HSE06) approach[115,116] with a mixing parameter of 0.25 and a screening parameter α of 0.2 Å^{-1}. To characterize the localization of the electronic states within the band gap and near the band edges, the IPR was calculated. Optical absorption was derived from the frequency-dependent dielectric function, $\varepsilon(\omega) = \varepsilon_1(\omega) + i\varepsilon_2(\omega)$, calculated within independent particle approximation in VASP. The imaginary part, $\varepsilon_2(\omega)$, is related to the optical absorption at a given frequency ω and is determined based on the electronic transitions of the hybrid functional solution. The real part of the complex dielectric function is obtained using Kramers−Kronig relations.

■ ASSOCIATED CONTENT

Supporting Information

The Supporting Information is available free of charge at https://pubs.acs.org/doi/10.1021/acs.chemmater.9b04257.

Experimental section, AFM, XRR plots and data, TFT architecture, output curves, bias stress data, MD simulations, UV−vis data, XPS data (PDF)

■ AUTHOR INFORMATION

Corresponding Authors

*E-mail: t-marks@northwestern.edu. (T.J.M.)
*E-mail: a-facchetti@northwestern.edu. (A.F.)
*E-mail: juliaem@mst.edu. (J.E.M.)
*E-mail: bedzyk@northwestern.edu. (M.J.B.)

ORCID

Qing Ma: 0000-0001-6530-9322
Wei Huang: 0000-0002-0973-8015
Binghao Wang: 0000-0002-9631-6901
Michael J. Bedzyk: 0000-0002-1026-4558
Antonio Facchetti: 0000-0002-8175-7958
Tobin J. Marks: 0000-0001-8771-0141

Present Address

#Laleh Avazpour, Electrical and Computer Engineering, University of Wisconsin−Madison, 1415 Engineering Drive, Madison 53706, Wisconsin, United States.

Notes

The authors declare no competing financial interest.

■ ACKNOWLEDGMENTS

We thank the Northwestern Univ. (NU) MRSEC Grant No. NSF-DMR 1720139 for support of this research. J.E.M. thanks NSF-DMREF Grant No. 1729779 for support and the XSEDE center for computational facilities. This work made use of the EPIC, Keck-II, and/or SPID facility(ies) of the Northwestern Univ. NU*ANCE* Center, which has received support from the Soft and Hybrid Nanotechnology Experimental Resource (NSF ECCS-1542205); the MRSEC program (NSF DMR-1720139) at the Materials Research Center; the International Institute for Nanotechnology (IIN); the Keck Foundation; and the State of Illinois, through the IIN. XRR measurements used the NU XRD Facility also supported by the NSF MRSEC grant. This work used the 5-BM-D beamline of the DuPont-Northwestern-Dow Collaborative Access Team (DND-CAT) located at Sector 5 of the Advanced Photon Source (APS). DND-CAT is supported by NU, E. I. DuPont de Nemours & Co., and The Dow Chemical Company. This research used resources of the APS, a U.S. Department of Energy (DOE) Office of Science User Facility operated for the DOE Office of Science by Argonne National Laboratory under Contract No. DE-AC02-06CH11357. A.S. thanks Dr. V. Hedge of the Prof. C. Wolverton group and Dr. S. L. Moffitt (SLAC) for helpful discussions.

■ ABBREVIATIONS

XPS, X-ray photoelectron spectroscopy; DSC, Differential scanning calorimetry; TGA, Thermogravimetric analysis; AFM, Atomic-force microscopy; GIXRD, Grazing incidence X-ray diffraction; XRR, X-ray reflectivity; TFT, Thin-film transistor; MD, Molecular dynamics; DFT, Density functional theory; EXAFS, Extended X-ray absorption fine structure; UV/

DOI: 10.1021/acs.chemmater.9b04257
Chem. Mater. 2020, 32, 805−820

vis/NIR, ultraviolet/visible/near-infrared; soln, solution; w/o, without; atom %, atom%; vs, versus

REFERENCES

(1) Nomura, K.; Ohta, H.; Takagi, A.; Kamiya, T.; Hirano, M.; Hosono, H. Room-temperature fabrication of transparent flexible thin-film transistors using amorphous oxide semiconductors. *Nature* **2004**, *432*, 488.

(2) Yu, X.; Smith, J.; Zhou, N.; Zeng, L.; Guo, P.; Xia, Y.; Alvarez, A.; Aghion, S.; Lin, H.; Yu, J.; Chang, R. P.; Bedzyk, M. J.; Ferragut, R.; Marks, T. J.; Facchetti, A. Spray-combustion synthesis: efficient solution route to high-performance oxide transistors. *Proc. Natl. Acad. Sci. U. S. A.* **2015**, *112*, 3217.

(3) Thomas, S. R.; Pattanasattayavong, P.; Anthopoulos, T. D. Solution-processable metal oxide semiconductors for thin-film transistor applications. *Chem. Soc. Rev.* **2013**, *42*, 6910.

(4) Labram, J. G.; Lin, Y. H.; Zhao, K.; Li, R. P.; Thomas, S. R.; Semple, J.; Androulidaki, M.; Sygellou, L.; McLachlan, M.; Stratakis, E.; Amassian, A.; Anthopoulos, T. D. Signatures of Quantized Energy States in Solution-Processed Ultrathin Layers of Metal-Oxide Semiconductors and Their Devices. *Adv. Funct. Mater.* **2015**, *25*, 1727.

(5) Yeon Kwon, J.; Kyeong Jeong, J. Recent progress in high performance and reliable n-type transition metal oxide-based thin film transistors. *Semicond. Sci. Technol.* **2015**, *30*, 024002.

(6) Tate, J.; Ju, H. L.; Moon, J. C.; Zakutayev, A.; Richard, A. P.; Russell, J.; McIntyre, D. H. Origin of p-type conduction in single-crystal CuAlO2. *Phys. Rev. B: Condens. Matter Mater. Phys.* **2009**, *80*, 165206.

(7) Pecunia, V.; Banger, K.; Sirringhaus, H. High-Performance Solution-Processed Amorphous-Oxide-Semiconductor TFTs with Organic Polymeric Gate Dielectrics. *Adv. Electron. Mater.* **2015**, *1*, 1400024.

(8) Wager, J. F.; Yeh, B.; Hoffman, R. L.; Keszler, D. A. An amorphous oxide semiconductor thin-film transistor route to oxide electronics. *Curr. Opin. Solid State Mater. Sci.* **2014**, *18*, 53.

(9) Yu, X.; Marks, T. J.; Facchetti, A. Metal oxides for optoelectronic applications. *Nat. Mater.* **2016**, *15*, 383.

(10) Yang, S.; Bak, J. Y.; Yoon, S. M.; Ryu, M. K.; Oh, H.; Hwang, C. S.; Kim, G. H.; Park, S. H. K.; Jang, J. Low-Temperature Processed Flexible In-Ga-Zn-O Thin-Film Transistors Exhibiting High Electrical Performance. *IEEE Electron Device Lett.* **2011**, *32*, 1692.

(11) Mo, Y. G.; Kim, M.; Kang, C. K.; Jeong, J. H.; Park, Y. S.; Choi, C. G.; Kim, H. D.; Kim, S. S. Amorphous-oxide TFT backplane for large-sized AMOLED TVs. *J. Soc. Inf. Disp.* **2011**, *19*, 16.

(12) Smith, J.; Zhang, W.; Sougrat, R.; Zhao, K.; Li, R.; Cha, D.; Amassian, A.; Heeney, M.; McCulloch, I.; Anthopoulos, T. D. Solution-processed small molecule-polymer blend organic thin-film transistors with hole mobility greater than 5 cm2/Vs. *Adv. Mater.* **2012**, *24*, 2441.

(13) Park, J. S.; Maeng, W.-J.; Kim, H.-S.; Park, J.-S. Review of recent developments in amorphous oxide semiconductor thin-film transistor devices. *Thin Solid Films* **2012**, *520*, 1679.

(14) Ma, H.; Acton, O.; Hutchins, D. O.; Cernetic, N.; Jen, A. K. Multifunctional phosphonic acid self-assembled monolayers on metal oxides as dielectrics, interface modification layers and semiconductors for low-voltage high-performance organic field-effect transistors. *Phys. Chem. Chem. Phys.* **2012**, *14*, 14110.

(15) Venkateshvaran, D.; Nikolka, M.; Sadhanala, A.; Lemaur, V.; Zelazny, M.; Kepa, M.; Hurhangee, M.; Kronemeijer, A. J.; Pecunia, V.; Nasrallah, I.; Romanov, I.; Broch, K.; McCulloch, I.; Emin, D.; Olivier, Y.; Cornil, J.; Beljonne, D.; Sirringhaus, H. Approaching disorder-free transport in high-mobility conjugated polymers. *Nature* **2014**, *515*, 384.

(16) Kim, M. G.; Kanatzidis, M. G.; Facchetti, A.; Marks, T. J. Low-temperature fabrication of high-performance metal oxide thin-film electronics via combustion processing. *Nat. Mater.* **2011**, *10*, 382.

(17) Gao, Z. Q.; Mi, B. X.; Xu, G. Z.; Wan, Y. Q.; Gong, M. L.; Cheah, K. W.; Chen, C. H. An organic p-type dopant with high thermal stability for an organic semiconductor. *Chem. Commun.* **2008**, *0*, 117.

(18) Ng, T. N.; Chabinyc, M. L.; Street, R. A.; Salleo, A. In *Bias Stress Effects in Organic Thin Film Transistors;* 45th Annual IEEE International Reliability Physics Symposium Proceedings; Phoenix, AZ, April 15−19, 2007; IEEE, 2007; pp 243.

(19) Fortunato, E.; Barquinha, P.; Martins, R. Oxide semiconductor thin-film transistors: a review of recent advances. *Adv. Mater.* **2012**, *24*, 2945.

(20) Hennek, J. W.; Smith, J.; Yan, A.; Kim, M. G.; Zhao, W.; Dravid, V. P.; Facchetti, A.; Marks, T. J. Oxygen ″getter″ effects on microstructure and carrier transport in low temperature combustion-processed a-InXZnO (X = Ga, Sc, Y, La) transistors. *J. Am. Chem. Soc.* **2013**, *135*, 10729.

(21) Choi, Y.; Kim, G. H.; Jeong, W. H.; Bae, J. H.; Kim, H. J.; Hong, J. M.; Yu, J. W. Carrier-suppressing effect of scandium in InZnO systems for solution-processed thin film transistors. *Appl. Phys. Lett.* **2010**, *97*, 162102.

(22) Qadri, S. B.; Kim, H. Synthesis of bulk In2O3-Sc2O3 and their transparent conducting oxide films. *J. Appl. Phys.* **2002**, *92*, 227.

(23) Shin, H. S.; Kim, G. H.; Jeong, W. H.; Du Ahn, B.; Kim, H. J. Electrical Properties of Yttrium-Indium-Zinc-Oxide Thin Film Transistors Fabricated Using the Sol-Gel Process and Various Yttrium Compositions. *Jpn. J. Appl. Phys.* **2010**, *49*, 03cb01.

(24) Paine, D. C.; Yaglioglu, B.; Beiley, Z.; Lee, S. Amorphous IZO-based transparent thin film transistors. *Thin Solid Films* **2008**, *516*, 5894.

(25) Jeong, S.; Jeong, Y.; Moon, J. Solution-processed zinc tin oxide semiconductor for thin-film transistors. *J. Phys. Chem. C* **2008**, *112*, 11082.

(26) Kim, H. S.; Kim, M. G.; Ha, Y. G.; Kanatzidis, M. G.; Marks, T. J.; Facchetti, A. Low-temperature solution-processed amorphous indium tin oxide field-effect transistors. *J. Am. Chem. Soc.* **2009**, *131*, 10826.

(27) Khim, D.; Lin, Y. H.; Nam, S.; Faber, H.; Tetzner, K.; Li, R.; Zhang, Q.; Li, J.; Zhang, X.; Anthopoulos, T. D. Modulation-Doped In2O3/ZnO Heterojunction Transistors Processed from Solution. *Adv. Mater.* **2017**, *29*, 1605837.

(28) Lin, Y. H.; Thomas, S. R.; Faber, H.; Li, R. P.; McLachlan, M. A.; Patsalas, P. A.; Anthopoulos, T. D. Al-Doped ZnO Transistors Processed from Solution at 120 degrees C. *Adv. Electron. Mater.* **2016**, *2*, 1600070.

(29) Hosono, H. Ionic amorphous oxide semiconductors: Material design, carrier transport, and device application. *J. Non-Cryst. Solids* **2006**, *352*, 851.

(30) Park, J. C.; Kim, S.; Kim, S.; Kim, C.; Song, I.; Park, Y.; Jung, U. I.; Kim, D. H.; Lee, J. S. Highly stable transparent amorphous oxide semiconductor thin-film transistors having double-stacked active layers. *Adv. Mater.* **2010**, *22*, 5512.

(31) Kamiya, T.; Hosono, H. Material characteristics and applications of transparent amorphous oxide semiconductors. *NPG Asia Mater.* **2010**, *2*, 15.

(32) Kamiya, T.; Nomura, K.; Hosono, H. Present status of amorphous In-Ga-Zn-O thin-film transistors. *Sci. Technol. Adv. Mater.* **2010**, *11*, 044305.

(33) Nathan, A.; Lee, S.; Jeon, S.; Robertson, J. Amorphous Oxide Semiconductor TFTs for Displays and Imaging. *J. Disp. Technol.* **2014**, *10*, 917.

(34) Kwon, J. Y.; Lee, D. J.; Kim, K. B. Review Paper: Transparent Amorphous Oxide Semiconductor Thin Film Transistor. *Electron. Mater. Lett.* **2011**, *7*, 1.

(35) Takagi, A.; Nomura, K.; Ohta, H.; Yanagi, H.; Kamiya, T.; Hirano, M.; Hosono, H. Carrier transport and electronic structure in amorphous oxide semiconductor, a-InGaZnO4. *Thin Solid Films* **2005**, *486*, 38.

(36) Cho, D. Y.; Song, J.; Na, K. D.; Hwang, C. S.; Jeong, J. H.; Jeong, J. K.; Mo, Y. G. Local structure and conduction mechanism in amorphous In-Ga-Zn-O films. *Appl. Phys. Lett.* **2009**, *94*, 112112.

DOI: 10.1021/acs.chemmater.9b04257
Chem. Mater. 2020, 32, 805−820

(37) Kimura, M.; Kamiya, T.; Nakanishi, T.; Nomura, K.; Hosono, H. Intrinsic carrier mobility in amorphous In-Ga-Zn-O thin-film transistors determined by combined field-effect technique. *Appl. Phys. Lett.* **2010**, *96*, 262105.
(38) Medvedeva, J. E.; Buchholz, D. B.; Chang, R. P. H. Recent Advances in Understanding the Structure and Properties of Amorphous Oxide Semiconductors. *Adv. Electron. Mater.* **2017**, *3*, 1700082.
(39) Moffitt, S. L.; Zhu, Q. M.; Ma, Q.; Falduto, A. F.; Buchholz, D. B.; Chang, R. P. H.; Mason, T. O.; Medvedeva, J. E.; Marks, T. J.; Bedzyk, M. J. Probing the Unique Role of Gallium in Amorphous Oxide Semiconductors through Structure-Property Relationships. *Adv. Electron. Mater.* **2017**, *3*, 1700189.
(40) Huang, W.; Zeng, L.; Yu, X. G.; Guo, P. J.; Wang, B. H.; Ma, Q.; Chang, R. P. H.; Yu, J. S.; Bedzyk, M. J.; Marks, T. J.; Facchetti, A. Metal Oxide Transistors via Polyethylenimine Doping of the Channel Layer: Interplay of Doping, Microstructure, and Charge Transport. *Adv. Funct. Mater.* **2016**, *26*, 6179.
(41) Yu, X.; Zeng, L.; Zhou, N.; Guo, P.; Shi, F.; Buchholz, D. B.; Ma, Q.; Yu, J.; Dravid, V. P.; Chang, R. P.; Bedzyk, M.; Marks, T. J.; Facchetti, A. Ultra-flexible, "invisible" thin-film transistors enabled by amorphous metal oxide/polymer channel layer blends. *Adv. Mater.* **2015**, *27*, 2390.
(42) Huang, W.; Guo, P.; Zeng, L.; Li, R.; Wang, B.; Wang, G.; Zhang, X.; Chang, R. P. H.; Yu, J.; Bedzyk, M. J.; Marks, T. J.; Facchetti, A. Metal Composition and Polyethylenimine Doping Capacity Effects on Semiconducting Metal Oxide-Polymer Blend Charge Transport. *J. Am. Chem. Soc.* **2018**, *140*, 5457.
(43) Mori, T.; Kajihara, K.; Kanamura, K.; Toda, Y.; Hiramatsu, H.; Hosono, H. Indium-Based Ultraviolet-Transparent Electroconductive Oxyfluoride InOF: Ambient-Pressure Synthesis and Unique Electronic Properties in Comparison with In2O3. *J. Am. Chem. Soc.* **2013**, *135*, 13080.
(44) Harada, J. K.; Charles, N.; Poeppelmeier, K. R.; Rondinelli, J. M. Heteroanionic Materials by Design: Progress Toward Targeted Properties. *Adv. Mater.* **2019**, *31*, 1805295.
(45) Kageyama, H.; Hayashi, K.; Maeda, K.; Attfield, J. P.; Hiroi, Z.; Rondinelli, J. M.; Poeppelmeier, K. R. Expanding frontiers in materials chemistry and physics with multiple anions. *Nat. Commun.* **2018**, *9*, 772.
(46) Shannon, R. D. Revised Effective Ionic-Radii and Systematic Studies of Interatomic Distances in Halides and Chalcogenides. *Acta Crystallogr., Sect. A: Cryst. Phys., Diffr., Theor. Gen. Crystallogr.* **1976**, *32*, 751.
(47) Wang, D. P.; Jiang, J. X.; Furuta, M. Investigation of Carrier Generation Mechanism in Fluorine-Doped n(+)-In-Ga-Zn-O for Self-Aligned Thin-Film Transistors. *J. Disp. Technol.* **2016**, *12*, 258.
(48) Qian, L. X.; Tang, W. M.; Lai, P. T. Improved Characteristics of InGaZnO Thin-Film Transistor by Using Fluorine Implant. *ECS Solid State Lett.* **2014**, *3*, P87.
(49) Jiang, J. X.; Toda, T.; Hung, M. P.; Wang, D. P.; Furuta, M. Highly stable fluorine-passivated In-Ga-Zn-O thin-film transistors under positive gate bias and temperature stress. *Appl. Phys. Express* **2014**, *7*, 114103.
(50) Qian, L. X.; Lai, P. T. Fluorinated InGaZnO Thin-Film Transistor With HfLaO Gate Dielectric. *IEEE Electron Device Lett.* **2014**, *35*, 363.
(51) Rahaman, A.; Billah, M. M.; Um, J. G.; Hasan, M. M.; Jang, J. Effect of Doping Fluorine in Offset Region on Performance of Coplanar a-IGZO TFTs. *IEEE Electron Device Lett.* **2018**, *39*, 1318.
(52) Jung, W. S.; Park, J. H.; Nainani, A.; Nam, D.; Saraswat, K. C. Fluorine passivation of vacancy defects in bulk germanium for Ge metal-oxide-semiconductor field-effect transistor application. *Appl. Phys. Lett.* **2012**, *101*, 072104.
(53) Ye, Z.; Wong, M. Characteristics of Thin-Film Transistors Fabricated on Fluorinated Zinc Oxide. *IEEE Electron Device Lett.* **2012**, *33*, 549.
(54) Seo, J. S.; Jeon, J. H.; Hwang, Y. H.; Park, H.; Ryu, M.; Park, S. H.; Bae, B. S. Solution-processed flexible fluorine-doped indium zinc oxide thin-film transistors fabricated on plastic film at low temperature. *Sci. Rep.* **2013**, *3*, 2085.
(55) Chang, J. J.; Lin, Z. H.; Lin, M.; Zhu, C. X.; Zhang, J.; Wu, J. S. Solution processed F doped ZnO (ZnO:F) for thin film transistors and improved stability through co-doping with alkali metals. *J. Mater. Chem. C* **2015**, *3*, 1787.
(56) Jeon, J. H.; Hwang, Y. H.; Jin, J.; Bae, B. S. Low-temperature aqueous solution processed fluorine-doped zinc tin oxide thin-film transistors. *MRS Commun.* **2012**, *2*, 17.
(57) Wang, B.; Zeng, L.; Huang, W.; Melkonyan, F. S.; Sheets, W. C.; Chi, L.; Bedzyk, M. J.; Marks, T. J.; Facchetti, A. Carbohydrate-Assisted Combustion Synthesis To Realize High-Performance Oxide Transistors. *J. Am. Chem. Soc.* **2016**, *138*, 7067.
(58) Wang, B. H.; Yu, X. G.; Guo, P. J.; Huang, W.; Zeng, L.; Zhou, N. J.; Chi, L. F.; Bedzyk, M. J.; Chang, R. P. H.; Marks, T. J.; Facchetti, A. Solution-Processed All-Oxide Transparent High-Performance Transistors Fabricated by Spray-Combustion Synthesis. *Adv. Electron. Mater.* **2016**, *2*, 1500427.
(59) Kim, M. G.; Hennek, J. W.; Kim, H. S.; Kanatzidis, M. G.; Facchetti, A.; Marks, T. J. Delayed ignition of autocatalytic combustion precursors: low-temperature nanomaterial binder approach to electronically functional oxide films. *J. Am. Chem. Soc.* **2012**, *134*, 11583.
(60) Kim, J. H.; Liang, P.-W.; Williams, S. T.; Cho, N.; Chueh, C.-C.; Glaz, M. S.; Ginger, D. S.; Jen, A. K. Y. High-Performance and Environmentally Stable Planar Heterojunction Perovskite Solar Cells Based on a Solution-Processed Copper-Doped Nickel Oxide Hole-Transporting Layer. *Adv. Mater.* **2015**, *27*, 695.
(61) Kang, Y. H.; Jeong, S.; Ko, J. M.; Lee, J. Y.; Choi, Y.; Lee, C.; Cho, S. Y. Two-component solution processing of oxide semiconductors for thin-film transistors via self-combustion reaction. *J. Mater. Chem. C* **2014**, *2*, 4247.
(62) Jung, J. W.; Chueh, C. C.; Jen, A. K. A Low-Temperature, Solution-Processable, Cu-Doped Nickel Oxide Hole-Transporting Layer via the Combustion Method for High-Performance Thin-Film Perovskite Solar Cells. *Adv. Mater.* **2015**, *27*, 7874.
(63) Hennek, J. W.; Kim, M. G.; Kanatzidis, M. G.; Facchetti, A.; Marks, T. J. Exploratory combustion synthesis: amorphous indium yttrium oxide for thin-film transistors. *J. Am. Chem. Soc.* **2012**, *134*, 9593.
(64) Bai, S.; Cao, M.; Jin, Y.; Dai, X.; Liang, X.; Ye, Z.; Li, M.; Cheng, J.; Xiao, X.; Wu, Z.; Xia, Z.; Sun, B.; Wang, E.; Mo, Y.; Gao, F.; Zhang, F. Low-Temperature Combustion-Synthesized Nickel Oxide Thin Films as Hole-Transport Interlayers for Solution-Processed Optoelectronic Devices. *Adv. Energy Mater.* **2014**, *4*, 1301460.
(65) Bae, E. J.; Kang, Y. H.; Han, M. J.; Lee, C. J.; Cho, S. Y. Soluble oxide gate dielectrics prepared using the self-combustion reaction for high-performance thin-film transistors. *J. Mater. Chem. C* **2014**, *2*, 5695.
(66) Yu, X.; Zhou, N.; Smith, J.; Lin, H.; Stallings, K.; Yu, J.; Marks, T. J.; Facchetti, A. Synergistic approach to high-performance oxide thin film transistors using a bilayer channel architecture. *ACS Appl. Mater. Interfaces* **2013**, *5*, 7983.
(67) Xu, W.; Cao, H.; Liang, L.; Xu, J. B. Aqueous Solution-Deposited Gallium Oxide Dielectric for Low-Temperature, Low-Operating-Voltage Indium Oxide Thin-Film Transistors: A Facile Route to Green Oxide Electronics. *ACS Appl. Mater. Interfaces* **2015**, *7*, 14720.
(68) Noh, H. K.; Chang, K. J.; Ryu, B.; Lee, W. J. Electronic structure of oxygen-vacancy defects in amorphous In-Ga-Zn-O semiconductors. *Phys. Rev. B: Condens. Matter Mater. Phys.* **2011**, *84*, 115205.
(69) Medvedeva, J. E.; Khanal, R. Long-range structural correlations in amorphous ternary In-based oxides. *Vacuum* **2015**, *114*, 142.
(70) King, P. D. C.; Veal, T. D.; Fuchs, F.; Wang, C. Y.; Payne, D. J.; Bourlange, A.; Zhang, H.; Bell, G. R.; Cimalla, V.; Ambacher, O.; Egdell, R. G.; Bechstedt, F.; McConville, C. F. Band gap, electronic structure, and surface electron accumulation of cubic and rhombohe-

DOI: 10.1021/acs.chemmater.9b04257
Chem. Mater. 2020, 32, 805−820

dralIn2O3. *Phys. Rev. B: Condens. Matter Mater. Phys.* **2009**, *79*, 205211.
(71) Fuchs, F.; Bechstedt, F. Indium-oxide polymorphs from first principles: Quasiparticle electronic states. *Phys. Rev. B: Condens. Matter Mater. Phys.* **2008**, *77*, 155107.
(72) Omran Alkhayatt, A. H.; Hussian, S. K. Fluorine highly doped nanocrystalline SnO2 thin films prepared by SPD technique. *Mater. Lett.* **2015**, *155*, 109.
(73) Elangovan, E.; Singh, M. P.; Ramamurthi, K. Studies on structural and electrical properties of spray deposited SnO2: F thin films as a function of film thickness. *Mater. Sci. Eng., B* **2004**, *113*, 143.
(74) Elangovan, E.; Ramamurthi, K. Studies on micro-structural and electrical properties of spray-deposited fluorine-doped tin oxide thin films from low-cost precursor. *Thin Solid Films* **2005**, *476*, 231.
(75) Benhaoua, A.; Rahal, A.; Benhaoua, B.; Jlassi, M. Effect of fluorine doping on the structural, optical and electrical properties of SnO2 thin films prepared by spray ultrasonic. *Superlattices Microstruct.* **2014**, *70*, 61.
(76) Arca, E.; Fleischer, K.; Shvets, I. V. An alternative fluorine precursor for the synthesis of SnO2:F by spray pyrolysis. *Thin Solid Films* **2012**, *520*, 1856.
(77) Ajili, M.; Castagne, M.; Turki, N. K. Spray solution flow rate effect on growth, optoelectronic characteristics and photoluminescence of SnO2:F thin films for photovoltaic application. *Optik* **2015**, *126*, 708.
(78) Acosta, D. R.; Estrada, W.; Castanedo, R.; Maldonado, A.; Valenzuela, M. A. Structural and surface studies of tin oxide films doped with fluorine. *Thin Solid Films* **2000**, *375*, 147.
(79) Moon, E. J.; Xie, Y.; Laird, E. D.; Keavney, D. J.; Li, C. Y.; May, S. J. Fluorination of epitaxial oxides: synthesis of perovskite oxyfluoride thin films. *J. Am. Chem. Soc.* **2014**, *136*, 2224.
(80) Wang, B.; Guo, P.; Zeng, L.; Yu, X.; Sil, A.; Huang, W.; Leonardi, M. J.; Zhang, X.; Wang, G.; Lu, S.; Chen, Z.; Bedzyk, M. J.; Schaller, R. D.; Marks, T. J.; Facchetti, A. Expeditious, scalable solution growth of metal oxide films by combustion blade coating for flexible electronics. *Proc. Natl. Acad. Sci. U. S. A.* **2019**, *116*, 9230.
(81) Banger, K. K.; Yamashita, Y.; Mori, K.; Peterson, R. L.; Leedham, T.; Rickard, J.; Sirringhaus, H. Low-temperature, high-performance solution-processed metal oxide thin-film transistors formed by a 'sol−gel on chip' process. *Nat. Mater.* **2011**, *10*, 45.
(82) Moulder, J. F.; Chastain, J. In *Handbook of x-ray photoelectron spectroscopy: a reference book of standard spectra for identification and interpretation of XPS data;* Chastain, J., Ed.; Physical Electronics Division Perkin-Elmer Corp.: Eden Prairie, MN, 1992.
(83) Varma, A.; Mukasyan, A. S.; Rogachev, A. S.; Manukyan, K. V. Solution Combustion Synthesis of Nanoscale Materials. *Chem. Rev.* **2016**, *116*, 14493.
(84) Moffitt, S. L.; Stallings, K. L.; Falduto, A. F.; Lee, W.; Buchholz, D. B.; Wang, B.; Ma, Q.; Chang, R. P. H.; Marks, T. J.; Bedzyk, M. J. Processing, Structure, and Transistor Performance: Combustion versus Pulsed Laser Growth of Amorphous Oxides. *ACS Appl. Electron. Mater.* **2019**, *1*, 548.
(85) Zhang, X.; Wang, B.; Huang, W.; Chen, Y.; Wang, G.; Zeng, L.; Zhu, W.; Bedzyk, M. J.; Zhang, W.; Medvedeva, J. E.; Facchetti, A.; Marks, T. J. Synergistic Boron Doping of Semiconductor and Dielectric Layers for High-Performance Metal Oxide Transistors: Interplay of Experiment and Theory. *J. Am. Chem. Soc.* **2018**, *140*, 12501.
(86) Donley, C.; Dunphy, D.; Paine, D.; Carter, C.; Nebesny, K.; Lee, P.; Alloway, D.; Armstrong, N. R. Characterization of indium-tin oxide interfaces using X-ray photoelectron spectroscopy and redox processes of a chemisorbed probe molecule: Effect of surface pretreatment conditions. *Langmuir* **2002**, *18*, 450.
(87) Kamiya, T.; Nomura, K.; Hirano, M.; Hosono, H. Electronic structure of oxygen deficient amorphous oxide semiconductor a-InGaZnO4-x: Optical analyses and first-principle calculations. *Phys. Status Solidi C* **2008**, *5*, 3098.
(88) Nomura, K.; Kamiya, T.; Hirano, M.; Hosono, H. Origins of threshold voltage shifts in room-temperature deposited and annealed a-In-Ga-Zn-O thin-film transistors. *Appl. Phys. Lett.* **2009**, *95*, 013502.
(89) Wu, C. H.; Chang, K. M.; Huang, S. H.; Deng, I. C.; Wu, C. J.; Chiang, W. H.; Lin, J. W.; Chang, C. C. The Effect of Thermal Annealing on the Properties of IGZO TFT Prepared by Atmospheric Pressure Plasma Jet. *ECS Trans.* **2012**, *45*, 189.
(90) Hwang, Y. H.; Jeon, J.-H.; Bae, B.-S. Post-Humid Annealing of Low-Temperature Solution-Processed Indium Based Metal Oxide TFTs. *Electrochem. Solid-State Lett.* **2011**, *14*, H303.
(91) Phi Hung, M.; Chare, C.; Nag, M.; de Jamblinne de Meux, A.; Genoe, J.; Steudel, S. Effect of High Oxygen Partial Pressure on Carrier Transport Mechanism in a-InGaZnO TFTs. *IEEE Trans. Electron Devices* **2018**, *65*, 2833.
(92) Yang, D. G.; Do Kim, H.; Kim, J. H.; Lee, S. W.; Park, J.; Kim, Y. J.; Kim, H.-S. The effect of sputter growth conditions on the charge transport and stability of In-Ga-Zn-O semiconductors. *Thin Solid Films* **2017**, *638*, 361.
(93) Meng, Y.; Liu, G.; Liu, A.; Song, H.; Hou, Y.; Shin, B.; Shan, F. Low-temperature fabrication of high performance indium oxide thin film transistors. *RSC Adv.* **2015**, *5*, 37807.
(94) Sabri, M. M.; Jung, J.; Yoon, D. H.; Yoon, S.; Tak, Y. J.; Kim, H. J. Hydroxyl radical-assisted decomposition and oxidation in solution-processed indium oxide thin-film transistors. *J. Mater. Chem. C* **2015**, *3*, 7499.
(95) de Jamblinne de Meux, A.; Bhoolokam, A.; Pourtois, G.; Genoe, J.; Heremans, P. Oxygen vacancies effects in a-IGZO: Formation mechanisms, hysteresis, and negative bias stress effects. *Phys. Status Solidi A* **2017**, *214*, 214.
(96) Khanal, R.; Buchholz, D. B.; Chang, R. P. H.; Medvedeva, J. E. Composition-dependent structural and transport properties of amorphous transparent conducting oxides. *Phys. Rev. B: Condens. Matter Mater. Phys.* **2015**, *91*, 205203.
(97) Labram, J. G.; Treat, N. D.; Lin, Y.-H.; Burgess, C. H.; McLachlan, M. A.; Anthopoulos, T. D. Energy Quantization in Solution-Processed Layers of Indium Oxide and Their Application in Resonant Tunneling Diodes. *Adv. Funct. Mater.* **2016**, *26*, 1656.
(98) Luo, Y.-R. In *Comprehensive handbook of chemical bond energies;* CRC Press: Boca Raton, FL, 2007.
(99) Buchholz, D. B.; Ma, Q.; Alducin, D.; Ponce, A.; Jose-Yacaman, M.; Khanal, R.; Medvedeva, J. E.; Chang, R. P. The Structure and Properties of Amorphous Indium Oxide. *Chem. Mater.* **2014**, *26*, 5401.
(100) Klauk, H. Organic thin-film transistors. *Chem. Soc. Rev.* **2010**, *39*, 2643.
(101) Ravel, B.; Newville, M. ATHENA, ARTEMIS, HEPHAESTUS: data analysis for X-ray absorption spectroscopy using IFEFFIT. *J. Synchrotron Radiat.* **2005**, *12*, 537.
(102) Kresse, G.; Hafner, J. Ab initiomolecular dynamics for liquid metals. *Phys. Rev. B: Condens. Matter Mater. Phys.* **1993**, *47*, 558.
(103) Kresse, G.; Hafner, J. Ab initiomolecular-dynamics simulation of the liquid-metal−amorphous-semiconductor transition in germanium. *Phys. Rev. B: Condens. Matter Mater. Phys.* **1994**, *49*, 14251.
(104) Kresse, G.; Furthmuller, J. Efficiency of ab-initio total energy calculations for metals and semiconductors using a plane-wave basis set. *Comput. Mater. Sci.* **1996**, *6*, 15.
(105) Kresse, G.; Furthmüller, J. Efficient iterative schemes for ab initiototal-energy calculations using a plane-wave basis set. *Phys. Rev. B: Condens. Matter Mater. Phys.* **1996**, *54*, 11169.
(106) Hohenberg, P.; Kohn, W. Inhomogeneous Electron Gas. *Phys. Rev.* **1964**, *136*, B864.
(107) Kohn, W.; Sham, L. J. Self-Consistent Equations Including Exchange and Correlation Effects. *Phys. Rev.* **1965**, *140*, 1133.
(108) Perdew, J. P.; Burke, K.; Ernzerhof, M. Generalized Gradient Approximation Made Simple. *Phys. Rev. Lett.* **1996**, *77*, 3865.
(109) Perdew, J. P.; Burke, K.; Ernzerhof, M. Generalized Gradient Approximation Made Simple [Phys. Rev. Lett. 77, 3865 (1996)]. *Phys. Rev. Lett.* **1997**, *78*, 1396.

DOI: 10.1021/acs.chemmater.9b04257
Chem. Mater. 2020, 32, 805−820

(110) Blochl, P. E. Projector augmented-wave method. *Phys. Rev. B: Condens. Matter Mater. Phys.* **1994**, *50*, 17953.
(111) Kresse, G.; Joubert, D. From ultrasoft pseudopotentials to the projector augmented-wave method. *Phys. Rev. B: Condens. Matter Mater. Phys.* **1999**, *59*, 1758.
(112) Hoppe, R. The Coordination Number— an"Inorganic Chameleon. *Angew. Chem., Int. Ed. Engl.* **1970**, *9*, 25.
(113) Hoppe, R.; Voigt, S.; Glaum, H.; Kissel, J.; Muller, H. P.; Bernet, K. A New Route to Charge-Distributions in Ionic Solids. *J. Less-Common Met.* **1989**, *156*, 105.
(114) Momma, K.; Izumi, F. VESTA 3for three-dimensional visualization of crystal, volumetric and morphology data. *J. Appl. Crystallogr.* **2011**, *44*, 1272.
(115) Heyd, J.; Peralta, J. E.; Scuseria, G. E.; Martin, R. L. Energy band gaps and lattice parameters evaluated with the Heyd-Scuseria-Ernzerhof screened hybrid functional. *J. Chem. Phys.* **2005**, *123*, 174101.
(116) Heyd, J.; Scuseria, G. E.; Ernzerhof, M. Hybrid functionals based on a screened Coulomb potential. *J. Chem. Phys.* **2003**, *118*, 8207.

DOI: 10.1021/acs.chemmater.9b04257
Chem. Mater. 2020, 32, 805−820